



## LJMU Research Online

**Kamperidis, VC, Papavasileiou, GS, Kamaris, GS and Vasdravellis, G**

**Seismic collapse of self-centering steel MRFs with different column base structural properties**

<http://researchonline.ljmu.ac.uk/id/eprint/13952/>

### Article

**Citation** (please note it is advisable to refer to the publisher's version if you intend to cite from this work)

**Kamperidis, VC, Papavasileiou, GS, Kamaris, GS and Vasdravellis, G (2020) Seismic collapse of self-centering steel MRFs with different column base structural properties. Journal of Constructional Steel Research, 175. ISSN 0143-974X**

LJMU has developed [LJMU Research Online](#) for users to access the research output of the University more effectively. Copyright © and Moral Rights for the papers on this site are retained by the individual authors and/or other copyright owners. Users may download and/or print one copy of any article(s) in LJMU Research Online to facilitate their private study or for non-commercial research. You may not engage in further distribution of the material or use it for any profit-making activities or any commercial gain.

The version presented here may differ from the published version or from the version of the record. Please see the repository URL above for details on accessing the published version and note that access may require a subscription.

For more information please contact [researchonline@ljmu.ac.uk](mailto:researchonline@ljmu.ac.uk)

<http://researchonline.ljmu.ac.uk/>

1                   **Seismic collapse of self-centering steel MRFs with different**  
2                   **column base structural properties**

3  
4                   **Vasileios C. Kamperidis<sup>a1</sup>, Georgios S. Papavasileiou<sup>b</sup>, George S. Kamaris<sup>c</sup> and**  
5                   **George Vasdravellis<sup>d</sup>**

6                   <sup>a</sup>School of Applied Sciences, Abertay University, Bell Street, Dundee, DD1 1HG, UK

7  
8                   <sup>b</sup>School of Architecture and Built Environment, University of Wolverhampton, Wulfruna Street,  
9                   Wolverhampton, WV1 1LY, UK

10  
11                   <sup>c</sup>Department of Civil Engineering, Liverpool John Moores University, Liverpool, L3 3AF, UK

12  
13                   <sup>d</sup>Institute for Infrastructure and Environment, Heriot-Watt University, Edinburgh, EH14 4AS, UK  
14

15                   **ABSTRACT**

16 The effect of the strength and stiffness characteristics of a previously proposed novel column  
17 base on the seismic performance and collapse capacity of steel self-centering moment-  
18 resisting frames is evaluated in this paper. This is done through three normalised parameters  
19 that represent the initial stiffness, post-yield stiffness, and strength of the column base, which  
20 can be independently adjusted. For these evaluations, a prototype steel building, which serves  
21 as a case study, is designed with sixteen different cases of a self-centering moment-resisting  
22 frame with different column base stiffness and strength characteristics (SC-MRF-CBs). A  
23 self-centering moment-resisting frame with conventional column bases and the same  
24 members and beam-column connections as those of the SC-MRF-CBs, named SC-MRF,  
25 serves as a benchmark frame. A set of 44 ground motions was used to conduct non-linear  
26 dynamic analyses and evaluate the seismic performance of the frames. Incremental dynamic  
27 analyses were also performed with the same ground motions set to evaluate the collapse  
28 capacity of the frames. Collapse capacity fragility curves and adjusted collapse margin ratios  
29 of the frames were derived and used for the comparison of the seismic risk of the frames. The

---

<sup>1</sup> Corresponding author, E-mail address: Vasileios.C.Kamperidis@gmail.com, ORCID ID number: 0000-0003-4893-7110.

30 results show that the new self-centering column base significantly improves the seismic  
31 performance of the SC-MRF, demonstrating the potential of the SC-MRF-CBs to be  
32 redesigned with smaller member sections. Moreover, the SC-MRF-CBs achieve significant  
33 reduction in collapse risk compared to the SC-MRF. Finally, the results show that increasing  
34 the base strength and stiffness improves the seismic performance and collapse capacity of the  
35 SC-MRF-CBs.

## 36 **KEYWORDS**

37 Column base; Self-centering; Collapse risk; Interstorey drifts and floor accelerations;  
38 Parametric investigation; Seismic resilience

## 39 **1 INTRODUCTION**

40 Column bases have a very important role in the seismic response of steel moment-resisting  
41 frames (MRFs) [1–5]. Eurocode 8 (EC8) [6] assumes that plastic hinges at the column base  
42 connection will offer increased rotational ductility compared to other plasticity mechanisms  
43 therein [7], such as column member plastic hinging. This strength-related code presumption  
44 has been questioned by Lignos and Krawinkler [8], who showed that the ductility of the  
45 column base plastic hinges may be compromised by local instabilities, leading to premature  
46 column failure. Moreover, Aviram et al. [5] and Ruiz-García and Kanvinde [3] showed that  
47 decreasing the initial stiffness of the base connections in low-rise buildings can change the  
48 height-wise drift distribution, leading to drift and damage concertation and eventually to  
49 collapse. Zareian and Kanvinde [2] showed that reducing the base fixity in low- to high-rise  
50 buildings can increase the members' force demands, alter the global plastic mechanism, and  
51 significantly reduce ductility, strength and collapse resistance. Torres-Rodas et al. [4] showed  
52 that increasing the base flexibility of three-dimensional framed buildings, increases their  
53 transient drifts and probabilities of collapse, while appreciably decreases their overstrength  
54 and ductility.

55 To address the deficiencies of MRFs under earthquakes, the self-centering MRFs (SC-MRFs)  
56 were developed, such as those, for example, proposed in [9–16]. The main practice for SC-  
57 MRFs is to use post-tensioned (PT) beam-column connections that utilise high-strength steel  
58 tendons to clamp the beams to the columns and, thus, provide a re-centering mechanism that  
59 can restore the initial geometry of the building up to a targeted seismic intensity. High-  
60 strength steel is used to ensure that the tendons remain elastic up to the targeted frame  
61 response. Therefore, in these SC-MRFs, the self-centering mechanism is provided through  
62 attaining a targeted elastic elongation capacity for their PT tendons. Other researchers [17,18]  
63 have provided self-centering mechanisms for their seismic-resilient MRFs by relying on fully  
64 recoverable plastic deformations for the self-centering components of their systems up to as  
65 targeted response level to eliminate the need for repair, i.e., by utilising superelastic shape  
66 memory alloys (SMAs) for their self-centering components. The SC-MRFs with high-  
67 strength PT tendons, which are of interest in this work, utilise energy dissipating devices  
68 (EDs) in their PT beam-column connections to dissipate seismic energy and reduce the  
69 seismic forces and accelerations [9]. These EDs can be easily removed or replaced, if  
70 damaged, which can improve building’s resilience [19,20]. Combining these techniques, SC-  
71 MRFs can minimize damage and residual drifts [10] and reduce peak drifts and floor  
72 accelerations [9,21].

73 Self-centering systems can offer an option of tuning the structural properties that fully define  
74 their seismic hysteretic response. These properties are the initial stiffness, post-yield stiffness,  
75 strength and energy dissipation. Different researchers have evaluated the effect of these  
76 properties on the seismic response of different types of self-centering systems. Christopoulos  
77 et al. [22,23] concluded that if adequate energy dissipation is provided in SDOF flag-shaped  
78 response systems, these could have similar or improved peak drift response compared to that  
79 of elastoplastic systems of the same initial stiffness and strength. It was highlighted, though,

80 that systems with self-centering response are prone to increased resonance vibration  
81 amplitudes when their post-yield stiffness ratio,  $\alpha$  (i.e., the ratio of the post-yield stiffness  
82 over the initial stiffness), is increased [23]. Subsequently, Christopoulos et al. [24] found that  
83 the maximum drift response of SDOF systems with self-centering response under the design  
84 basis earthquake (DBE) [6] slightly decreases for increasing values of their post-yield  
85 stiffness. Interestingly, this effect was reversed for the collapse prevention seismic  
86 performance level – a finding fundamentally opposite to what applies in elastoplastic  
87 systems. Karavasilis and Seo [25] concluded that increasing the strength and adding damping  
88 in self-centering SDOF systems, generally decreases their peak total accelerations and  
89 displacements. In contrast, Cimellaro [26] suggested that the drift response of a structure may  
90 be improved by adopting lower lateral strength combined with higher damping ratios. Chou  
91 and Chen [27] investigated the performance of SC-MRFs with either fixed or self-centering  
92 column bases under the DBE and maximum considered earthquake (MCE) [28]. However,  
93 they did not assess the effect of the base strength, stiffness and energy dissipation on the  
94 seismic response of their investigated systems.

95 SC-MRFs with conventional column bases still cannot fully avoid structural damage and  
96 residual drifts because of the plastic hinges developed at their column bases [9,10,27,29]. To  
97 address this issue, SC-MRFs with self-centering column bases with replaceable/repairable  
98 EDs (SC-MRF-CBs) were developed [27,29–33]. SC-MRF-CBs can eliminate damage at  
99 their column bases and, thus, exhibit negligible residual drifts. Kamperidis et al. [29] have  
100 shown that these systems significantly reduce the peak drifts compared to their correspondent  
101 SC-MRFs, i.e., the frame with the same PT beam-column connections and same members  
102 with the SC-MRF-CB, but with conventional rigid and full-strength column bases. In  
103 addition, the design procedure proposed in [29] has the ability to fine-tune in a controlled  
104 manner the strength, stiffness and hysteretic behaviour of a SC-MRF-CB, keeping these

105 parameters uncoupled. Thus, one can design an SC-MRF-CB adjusting these parameters in  
106 such a way that its seismic response can be enhanced. However, an extensive and thorough  
107 parametric study on the effects of these parameters to the seismic response of the SC-MRF-  
108 CBs is still missing.

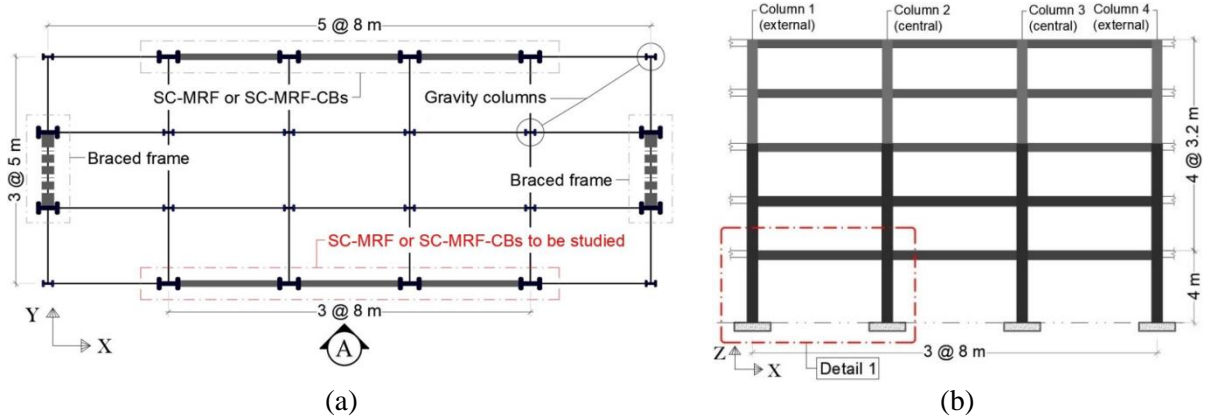
109 Moreover, the performance-based design approach of modern structural codes [28,34]  
110 mandates that buildings should be assessed against collapse as an extra measure of safety for  
111 human life, on the top of satisfying the traditional force and displacement requirements of the  
112 structural codes (e.g., EC8 [6]). This triggered research towards the collapse assessment of  
113 self-centering systems. In line with this, Tzimas et al. [35] found that the collapse capacity of  
114 SC-MRFs subjected to both far- and near-fault earthquakes, can be significantly improved by  
115 adding viscous dampers. However, the collapse risk of the SC-MRF-CBs and their potential  
116 to improve the collapse capacity of seismic-resistant steel buildings has never been evaluated.

117 This paper investigates the potential of SC-MRF-CBs equipped with the novel column base  
118 proposed in the work of Kamperidis et al. [29] to further improve the seismic performance  
119 and reduce the collapse risk of earthquake-resilient steel buildings equipped with SC-MRFs.  
120 The collapse risk of these new systems has never been assessed before and, so, it is of  
121 particular importance to investigate whether they attain a better or worse collapse behaviour  
122 compared to the SC-MRF. By comparing both the seismic performance and collapse risk of  
123 the SC-MRF-CBs with those of the SC-MRF, the performance of the former can be evaluated  
124 against all the performance criteria modern structural codes demand. As such, it can be  
125 concluded whether the SC-MRF-CBs can provide the potential to be designed for smaller  
126 steel members as compared to those of the SC-MRF. However, the explicit consideration of  
127 an SC-MRF-CB system with smaller cross-section than those of the SC-MRF is out of the  
128 scope of this work. Moreover, the mainstream approach for the SC-MRFs is to be designed  
129 for similar strength and initial stiffness with their correspondent conventional MRF [10,36],

130 referred to as correspondent MRF. Besides, due to the specific configuration of their PT  
131 beam-column connections, SC-MRFs do not allow for flexible stiffness and strength frame  
132 adjustments. For that reason, SC-MRFs are rather restricted to adhere to the above design  
133 approach. In contrast, the self-centering column bases allow for the controlled adjustment of  
134 all the structural properties that are necessary to fully determine their hysteretic behaviour to  
135 targeted predefined levels through mathematical formulas [29]. This base structural  
136 properties' control mechanism enables the adjustment of the stiffness and strength of the SC-  
137 MRF-CBs. An enhanced design procedure (compared to that in [29]) for the self-centering  
138 column bases is also proposed. This work thoroughly and methodologically investigates for  
139 the first time the effects of all the aforementioned base structural properties on the seismic  
140 performance and collapse capacity of the SC-MRF-CBs for a given level of energy  
141 dissipation in their bases. The base structural properties in question are the initial stiffness,  
142 post-yield stiffness, and strength, represented through three normalised factors, which are  
143 described next (Section 3.1). For this scope, a prototype steel building was designed that  
144 comprises different seismic-resistant frames: i.e., an SC-MRF and sixteen SC-MRF-CBs with  
145 different base stiffness and strength characteristics. The frames were modelled in OpenSees,  
146 where material and geometrical nonlinearities were taken into account, along with strength  
147 and stiffness degradation. A set of 44 ground motions, scaled to three code-prescribed  
148 seismic intensity levels [6,28], was used to conduct dynamic analyses and evaluate the  
149 seismic performance of the frames. In addition, incremental dynamic analyses (IDAs) were  
150 performed with the same set of ground motions to evaluate the collapse capacity of the  
151 frames. The collapse capacity fragility curves and the adjusted collapse margin ratio of the  
152 frames were derived and used for the comparison of the seismic risk of the frames.

153 **2 PROTOTYPE BUILDING**

154 The 5- by 3-bay, five-storey prototype steel building of [29], depicted in Figure 1, is utilised  
 155 in this work. Figure 1 shows the two identical braced frames in the  $Y$  direction and two  
 156 identical seismic-resistant frames in the  $X$  direction the building has at its perimeter. The  
 157 building has ductile non-structural elements and thus, the maximum interstorey drift ratio,  
 158  $\theta_{s,max}$ , must be less than 0.75% under the frequent occurred earthquake (FOE) in accordance  
 159 with EC8 [6]. The design spectrum of EC8 [6] with peak ground acceleration equal to 0.35g  
 160 and ground type B was used for the design of the frame under the DBE.

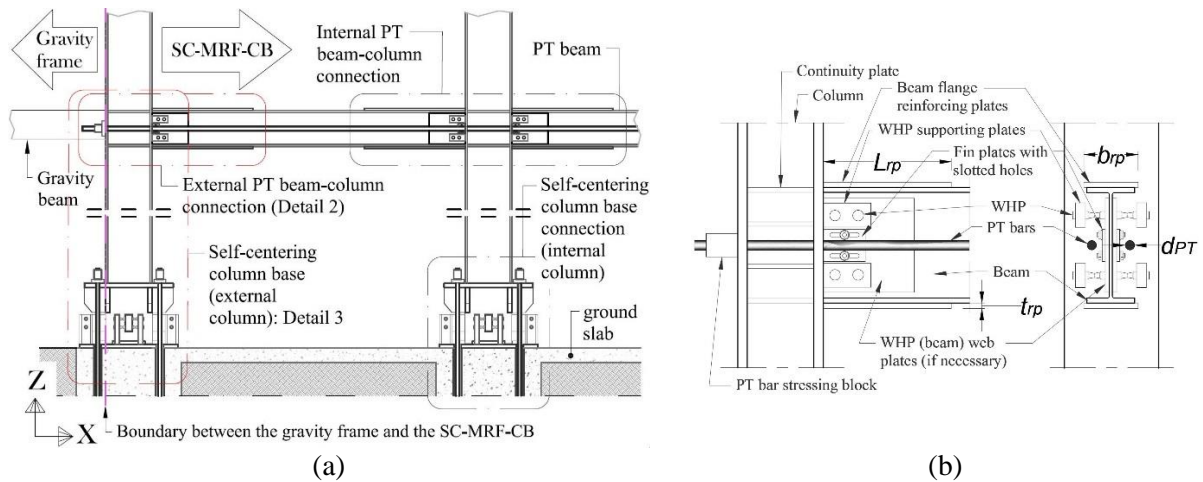


161 Figure 1 (a) Plan view; and (b) Elevation A of the prototype building.

162 Only the seismic-resistant frame of Elevation A of the prototype building, shown in Figure  
 163 1(b), is studied in this work. The frame of interest was designed as: (a) an SC-MRF,  
 164 following the design procedure of [10], to serve as the benchmark frame of this work; and (b)  
 165 sixteen different SC-MRF-CBs with the self-centering column bases proposed in [29], having  
 166 different base stiffness and strength characteristics but the same energy dissipation. The SC-  
 167 MRF and all SC-MRF-CBs have the same beams, columns and PT beam-column  
 168 connections. The design characteristics of the members and PT beam-column connections of  
 169 the SC-MRF are those described in [35]. Figure 2(a) illustrates the bottom-left part of an SC-  
 170 MRF-CB in Elevation A of the prototype building. The configurations of an external and  
 171 internal (central) PT beam-column connection of the frames are depicted in Figure 2(a).  
 172 Figure 2(b) shows a close-up view and the notation of these connections. The design



174 procedure proposed in [29] was used for the design of the self-centering column bases of the  
 175 SC-MRF-CBs.



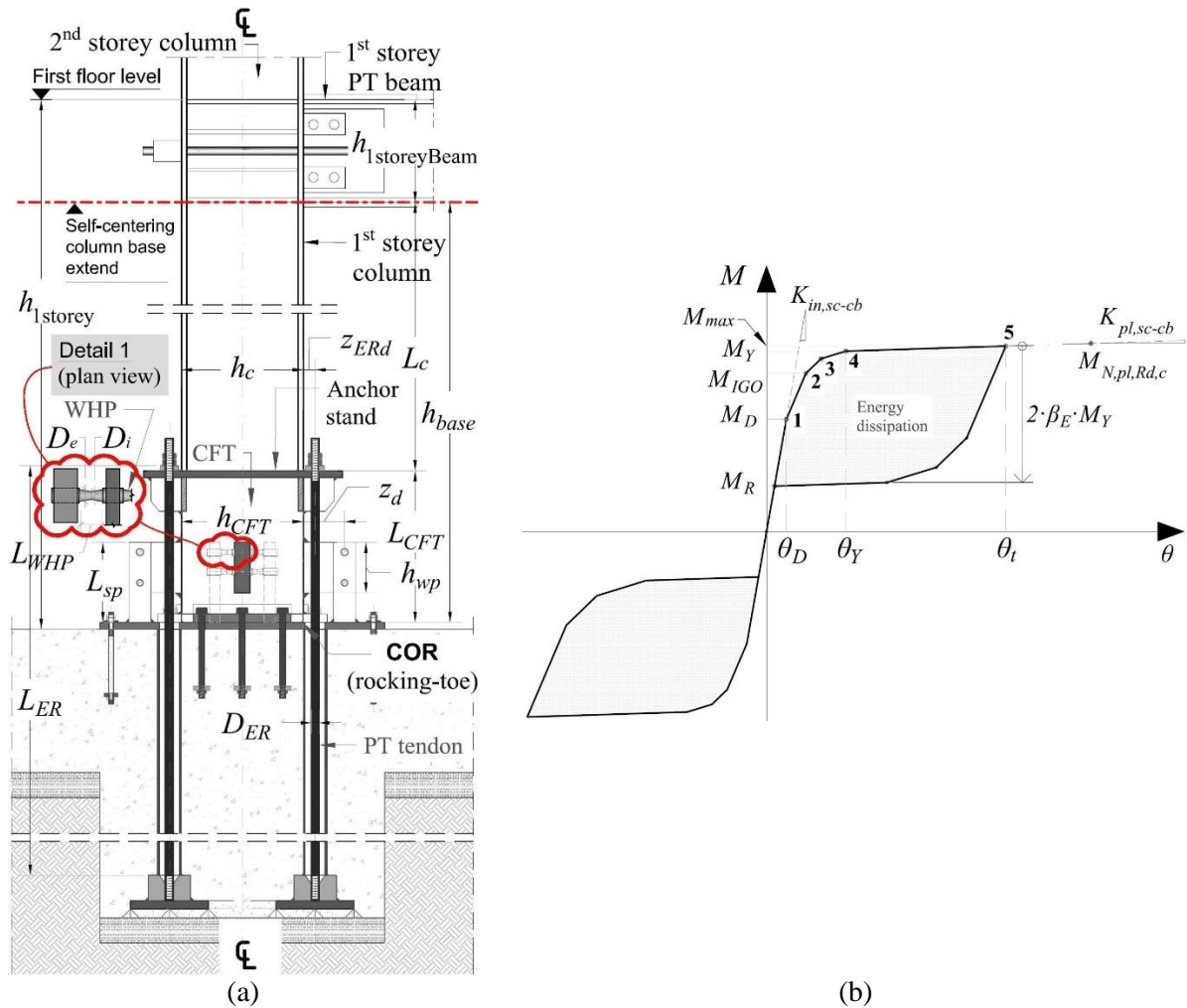
176 Figure 2 Close-up view of: (a) the bottom-left part of the SC-MRF-CB in Elevation A of the prototype  
 177 building (Detail 1 in Figure 1(b)); and (b) PT beam-column connection at an external column with its  
 178 notation (Detail 2 in Figure 2(a)).  
 179

180 The web hourglass pins (WHPs) described in [13] were utilised as EDs in the column bases  
 181 of the SC-MRF-CBs. The material of the WHPs was duplex stainless steel and its properties  
 182 were as follows, as per [14]: yield stress equal to 543 MPa; ultimate stress equal to 778 MPa;  
 183 elongation at fracture 34.25%; and Young's modulus equal to 227.848 GPa. The material for  
 184 the multi-wire tendons of the self-centering column bases was the low-relaxation Grade 270  
 185 steel material of ASTM A416 [37] with yield strength of 1676 MPa; ultimate tensile strength  
 186 of 1860 MPa; Young's modulus equal to 195 GPa; and ultimate elongation 3.5%. This  
 187 material, used in [38] and [39], is utilised in Section **Error! Reference source not found.** for  
 188 the fracture modelling of the tendons.

### 189 3 DESIGN CASES

190 Sixteen SC-MRF-CB design cases with different values for the strength, initial stiffness, and  
 191 post-yield stiffness of their self-centering column bases are employed for the parametric  
 192 study of this work. Thus, each self-centering column base employs a unique combination of  
 193 values for these three base structural properties. There are three values of strength, three  
 194 values of initial stiffness and five values of post-yield stiffness that are combined to form

195 these sixteen combinations in the self-centering column bases. These values cover the whole  
196 range of feasible values that can be achieved each base structural property when designing  
197 the self-centering column utilising the design procedure proposed in [29]. The three ranges of  
198 feasible values of the base structural properties are delimited by the given column cross-  
199 section and column design loads, which serve as input for the aforementioned design  
200 procedure [29]. The column and its design loads are derived from the elastic analysis and  
201 design of the correspondent MRF, from which the SC-MRF-CBs' designs stem [29]; this will  
202 be further explained next (Section 3.2). By examining self-centering column bases with base  
203 structural properties that span the whole range of their feasible values, the limits of the  
204 distinct effect of each one of these properties on the seismic response and collapse capacity of  
205 the SC-MRF-CBs can effectively be determined. The notation of the self-centering column  
206 bases can be seen in Figure 3(a). Each self-centering column base is considered to be a  
207 cantilevered assembly that comprises the self-centering low-damage column base connection,  
208 proposed in [29], and the steel column member of the first storey of the frame (Figure 3(a)).  
209 The self-centering column base connections are determined by the height of the concrete-  
210 filled tube (CFT) (seen in Figure 3(a)),  $L_{CFT}$ . The steel columns extend from the top of their  
211 self-centering base connections up to the lower limit of the panel zones of the first-storey PT  
212 beam-column connections. This limit is the level of the bottom flanges of the first-storey PT  
213 beams, as indicated by the red dashed line in Figure 3(a). The steel columns are determined  
214 by their length,  $L_c$ , as it is shown in Figure 3(a).



215 Figure 3 Self-centering column base: (a) configuration (Detail 3 in Figure 2(a)) and notation; and (b)  
 216 theoretical moment ( $M$ )-rotation ( $\theta$ ) behaviour for an assumed clockwise bending moment and axial  
 217 force.  
 218

219 The rationale for considering this specific cantilevered assembly configuration as the means  
 220 of assessing the base stiffness and strength of the SC-MRF-CBs is that it exclusively includes  
 221 the only two elements that change in the whole configuration of the SC-MRF-CBs, i.e., the  
 222 base connection and its connecting steel first-storey column. All the other parts of the frames  
 223 are the same as those of the SC-MRF. Similar approaches have been adopted in previous  
 224 relevant research [40]. Such an approach facilitates the large computational demands of this  
 225 work. The theoretical moment ( $M$ )-rotation ( $\theta$ ) behaviour of the self-centering column bases  
 226 can be seen in Figure 3(b). In this figure,  $\theta$  is the chord rotation of the self-centering column  
 227 bases, defined as the lateral displacement at the top of the column divided by the total height

228 of the column bases,  $h_{base}$ . Thus,  $h_{base}$  is related with the geometry of the frame through the  
229 following relation:

$$230 \quad h_{base} = h_{1storey} - h_{1storeyBeam} \quad (1)$$

231 where  $h_{1storey}$  is the total height of the first storey and  $h_{1storeyBeam}$  is the cross-sectional depth of  
232 the beams of the first floor.

### 233 3.1 Investigated base structural properties

234 The investigated structural properties of the self-centering column bases (or simply base  
235 structural properties) that are studied in this work are their strength,  $M_{IGO}$ , initial stiffness,  
236  $K_{in,sc-cb}$ , and post-yield stiffness,  $K_{pl,sc-cb}$ , which are described in Figure 3(b).  $M_{IGO}$  is the  
237 moment at the first yielding of the WHPs of the self-centering column base connection  
238 (Figure 3(b)).  $M_{IGO}$  is considered to represent the flexural strength of the self-centering  
239 column bases because the strength of a system with metallic fuses should correspond to the  
240 point where the first yielding of its structural fuses occurs [41]. The self-centering column  
241 base allows the controlled adjustment of these base structural properties by utilising the  
242 analytical expressions that are presented next. To uncouple the research findings of this work  
243 from the specific design characteristics of the frames studied herein (e.g., the size of the first-  
244 storey columns, the cross-sectional depth of which, denoted as  $h_c$  (see Figure 3(a)), and its  
245 plastic moment of resistance,  $M_{N,pl,Rd,c}$  (described in Eq. (3), below), are of interest in this  
246 study), the base structural properties are represented by the following normalised parameters:  
247 (a) the strength ratio,  $\eta$ ; (b) the normalised initial base stiffness factor,  $\beta_{base}$ ; and (c) the post-  
248 yield stiffness ratio,  $\alpha$ . Thus, the findings of this work can be extended to any SC-MRF-CB  
249 that is designed as per the design procedure proposed in [29].

250 Likewise previous research [25,42], the energy dissipation factor,  $\beta_E$ , is utilised to control the  
251 energy dissipation in all sixteen self-centering column bases.  $\beta_E$  was selected to take the

252 same, near-maximum allowable value to allow the self-centering behaviour of the column  
 253 bases and maximise their seismic energy dissipation. Thus,  $\beta_E$  was not included in the  
 254 parametric study. Based on previous relevant research [22,23,43], it was hypothesized that by  
 255 maximising the energy dissipation at the column bases, the seismic response and collapse  
 256 capacity of the SC-MRF-CBs would be optimally improved. Because the upper bound of  $\beta_E$   
 257 equals 0.5 [25,42],  $\beta_E$  was conservatively taken equal to 0.48 in all self-centering column  
 258 bases. The energy dissipation in each self-centering column base is due to the energy  
 259 dissipated by the WHPs up to the target base rotation,  $\theta_t$  (Figure 3(b)); the steel columns were  
 260 intended to remain elastic and not contribute to the energy dissipation of the self-centering  
 261 column bases. For this research,  $\theta_t$  was conservatively chosen to be equal to the rotation  
 262 capacity limit of EC8 for ductility class high MRFs, i.e., 0.035 radians [6]. This implies that  
 263 no strength and stiffness deterioration was expected to take place up to  $\theta_t$ .  $\beta_E$  was defined as:

$$264 \quad \beta_E = \frac{M_Y - M_D}{M_Y} \quad (2)$$

265 where  $M_Y$  is the moment of the self-centering column bases when all WHPs have reached  
 266 their elastic limit; and  $M_D$  is the decompression moment of the self-centering connection, i.e.,  
 267 the moment at which the gap at the rocking interface of the column base opens [10,29]. These  
 268 characteristic moments, along with their corresponding rotations, can be seen in Figure 3(b).

269 The strength factor,  $\eta$ , was defined as:

$$270 \quad \eta = \frac{M_{IGO}}{M_{N,pl,Rd,c}} \quad (3)$$

271 where  $M_{IGO}$  is the moment at the first yielding of the WHPs of the self-centering column base  
 272 connection;  $M_{N,pl,Rd,c}$  is the plastic moment of resistance of the column.  $M_{N,pl,Rd,c}$  accounts for  
 273 interaction with the design axial force,  $N_{Ed}$ , and the overstrength of the connections materials  
 274 and for other material effects, in accordance with EC8 [6] and Eurocode 3 (EC3) [44]

275 provisions.  $N_{Ed}$  is the axial force derived from the analysis of the correspondent MRF for the  
 276 gravity loads combination of actions [29]. The strength factor  $\eta$  consists a measure of the  
 277 strength of the base connection but can represent the strength of the whole self-centering  
 278 column base because the former is the only part of the latter that is expected to yield up to  $\theta_t$ .  
 279 The concept that the strength factor  $\eta$  consists a measure of the column bases' strength was  
 280 adopted on the basis that it relates the yield strength of the base connections with that of the  
 281 column member. This is in line with the relevant provisions of Eurocode 3 [45] that classify  
 282 moment-resisting connections with respect to their strength by comparing the strength of the  
 283 connections with the strength of their connecting members. Previous research on PT beam-  
 284 column connections [10] has set out an upper limit for  $\eta$  equal to unity. The parametric  
 285 investigation of this work shown that to achieve self-centering and damage-control behaviour  
 286 up to  $\theta_t$ , only values of  $\eta$  below 0.45 were capable of yielding self-centering column base  
 287 designs with initial and post-yield stiffness within their feasible range of values; these latter  
 288 two base structural properties were controlled through their normalised factors,  $\beta_{base}$  and  $\alpha$ ,  
 289 respectively, described next. For that reason, the three values of  $\eta$  this work examined were  
 290 0.30, 0.35 and 0.40.

291 The normalised initial base stiffness factor,  $\beta_{base}$ , was defined as:

$$292 \quad \beta_{base} = \frac{K_{in,sc-cb}}{K_{in,conv}} \quad (4)$$

293 where  $K_{in,conv}$  is the initial (elastic) flexural stiffness of a cantilever-fixed steel column of total  
 294 height equal to  $h_{base}$ ; and  $K_{in,sc-cb}$  the initial stiffness of a self-centering column base, assumed  
 295 equal to the elastic flexural stiffness of the steel cantilevered column on the top of the self-  
 296 centering column base connection,  $K_{el,col}$ , since the initial stiffness of the latter connection is  
 297 taken as infinite [29]. Thus,  $K_{el,col}$  is calculated for a column height of  $L_c$ . For the self-

298 centering column bases under investigation, the three  $\beta_{base}$  values examined were 133%,  
 299 167% and 200%.

300 The post-yield stiffness ratio,  $\alpha$ , was defined according to the following relation:

$$301 \quad \alpha = \frac{K_{pl,sc-cb}}{K_{in,sc-cb}} \quad (5)$$

302 where  $K_{pl,sc-cb}$  is the post-yield stiffness of the self-centering column base, defined as:

$$303 \quad K_{pl,Sc-Bc} = \frac{K_{pl,sc-cb} \cdot K_{el,col}}{K_{pl,sc-cb} + K_{el,col}} \quad (6)$$

304 where  $K_{pl,sc-cb}$  is the post-yield stiffness of the self-centering column base connection, which  
 305 was determined by the following relation [29]:

$$306 \quad K_{pl,sc-cb} = K_{fe} \cdot \left( \lambda \cdot n_{WHPu} \cdot z_u^2 + \lambda \cdot n_{WHPc} \cdot z_c^2 + \lambda \cdot n_{WHPd} \cdot z_d^2 \right) + K_{ER} \cdot \left( n_{ERu} \cdot z_{ERu}^2 + n_{ERd} \cdot z_{ERd}^2 \right) \quad (7)$$

307 where  $k_{fe}$  is the elastic stiffness of a single WHP [29];  $\lambda$  equals 2% according to [29];  $n_{WHPu}$   
 308 and  $n_{WHPd}$  are the numbers of the WHPs at the gap-opening and rocking-toe side of the self-  
 309 centering column base connections (the rocking toe coincides with the centre of rotation of  
 310 the connection (COR), as it is seen in Figure 3(a) for an assumed clockwise moment);  $n_{WHPc}$   
 311 the number of the central WHPs;  $z_u$ ,  $z_d$  and  $z_c$ , the lever arms of the WHPs at the gap-opening  
 312 side, rocking-toe side and that of the central WHPs, respectively;  $K_{ER}$  is the elastic axial  
 313 stiffness of each tendon, equal to  $E_{ER} \cdot A_{ER} / L_{ER}$ , with  $E_{ER}$ ,  $A_{ER}$  and  $L_{ER}$  the tendon's material  
 314 Young's modulus, cross-sectional area and length, respectively; and  $n_{ERu}$  and  $n_{ERd}$ , and  $z_{ERu}$   
 315 and  $z_{ERd}$  the number and lever arms of the PT tendons at the gap-opening and rocking-toe side  
 316 of the self-centering column base, respectively. The lever arms  $z_d$  and  $z_{ERd}$ , are defined in  
 317 Figure 3(a). The lever arms  $z_u$  and  $z_{ERu}$  were derived by adding to  $z_d$  and  $z_{ERd}$  the cross-  
 318 sectional depth of the CFT,  $h_{CFT}$ , respectively.  $z_c$  equals  $h_{CFT}/2$ . Five different values of  $\alpha$   
 319 were examined in this work, i.e., 5%, 10%, 15%, 20% and 24.5%. The value of 24.5% was

320 the maximum value of  $\alpha$  obtained for the given level of strength and initial stiffness of the  
321 relevant self-centering column base. This is in agreement with the maximum achievable limit  
322 of  $\alpha$  for real flag-shaped response systems, determined to about 25%, proposed by Wiebe and  
323 Christopoulos [46].

### 324 3.2 Self-centering column base design procedure

325 This section presents the design procedure utilised to derive the sixteen self-centering column  
326 base designs that are investigated in this work. The design procedure is that described in the  
327 work of Kamperidis et al. [29], with the only difference being that – in this work – the  
328 investigated base structural properties are given pre-selected values utilising Eq. (2) through  
329 (7) of Section 3.1. Pre-selecting these values, reduces the number of unknowns to be  
330 determined (as compared to the approach adopted in [29]), significantly facilitating the  
331 design process. To minimize repetition since the design procedure in [29] has been presented  
332 therein in detail, the design approach adopted in this work presents only limited mathematical  
333 formulas from [29].

334 To initiate the design procedure, the following input quantities are required: the column axial  
335 force,  $N_{Ed}$ ; the column cross-section, so that its cross-sectional depth,  $h_c$ , and plastic moment  
336 of resistance,  $M_{N,plRd,c}$ , are determined; and the target base rotation,  $\theta_t$ . The design procedure  
337 comprises the following steps:

#### 338 Step 1: Design the tendons

- 339 (a) Select a value for  $\beta_{base}$  and calculate  $K_{in,sc-cb}$  from Eq. (4). From  $K_{in,sc-cb}$ ,  $L_c$  is derived  
340 utilising the relevant elastic flexural stiffness formula from mechanics (Section 3.1).  
341 From Figure 3(a) and given the resulted  $L_c$  value,  $h_{CFT}$  can be derived.
- 342 (b) Select a value for the strength factor,  $\eta$ . From Eq. (3)  $M_{IGO}$  can then be derived.



- 343 (c) Select a value for the ratio  $M_D/M_{IGO}$  so that is it larger than 0.5, but as closer as it gets  
 344 to that latter value. This is to ensure self-centering capability but also to maximize  
 345 energy dissipation. Thus,  $M_D$  is derived.
- 346 (d) Select a number,  $n_{ERu}=n_{ERd}$ , and a lever arm for the tendons, e.g.,  $z_{ERd}$  ( $z_{ERu}$  can be  
 347 determined as per Section 3.1). It is suggested that four tendons are placed at the  
 348 corners of the anchor stand, which is the elevated stiff plate welded on the top of the  
 349 CFT (see Figure 3(a)); i.e.,  $n_{ERu}=n_{ERd}=2$ . Then, calculate the initial post-tensioning  
 350 force at each tendon,  $T$ , as per Eq. (2) of Kamperidis et al. [29].
- 351 (e) Select an appropriate high-strength steel grade material for the tendons, e.g., Grade  
 352 270 steel material of ASTM A416, to ensure a high yield strength,  $f_{y,ER}$ , for the  
 353 tendons, and assume a diameter for them,  $D_{ER}$  (this determines  $A_{ER}$ ). Then, utilize Eq.  
 354 (3) of [29] to calculate  $L_{ER}$ . Also, approximate the moment contribution of the tendons  
 355 for the characteristic rotation,  $\theta_2$ , denoted as  $M_{ER}(\theta_2)$ , as per Eq. (7) of [29].  $\theta_2$  is the  
 356 rotation at which the first WHP of the self-centering column base yields.  $M_{ER}(\theta_2)$  is to  
 357 be used next.

358 Step 2: Design the WHPs

- 359 (a) Select a number for the WHPs at each side of the self-centering column base (e.g.,  
 360  $n_{WHPd}$ ). It is suggested that two WHPs are placed at all sides of the column base; this  
 361 is for construction practicality and to ensure that the column base control its structural  
 362 properties over both of its main axes [29]; i.e.,  $n_{WHPd}=n_{WHPc}=n_{WHPu}=2$ . Also, select a  
 363 lever arm for the WHPs, e.g.,  $z_d$  ( $z_u$  and  $z_c$  can be determined as per Section 3.1).  
 364 Then, calculate the yield strength of a single WHP,  $F_{y,WHPi}$ , as per Eq. (5) of [29],  
 365 utilising  $M_{ER}(\theta_2)$  from Step 1(e). The internal diameter of the WHPs,  $D_i$  (described in  
 366 Detail 1 of Figure 3(a)), can then be calculated from the following relation as per  
 367 [10,29]:

368 
$$D_i = \sqrt{\frac{2 \cdot F_{y,WHP,i} \cdot \sqrt{3}}{\pi \cdot f_{y,WHP}}} \quad (8)$$

369 where  $f_{y,WHP}$  is the yield strength of the material of the WHPs.

370 (b) Select a value for  $\alpha$ , and based on Eq. (5) and the value of  $K_{in,sc-cb}$  derived from Step  
 371 1(a), calculate  $K_{pl,sc-cb}$ . Based on the  $K_{pl,sc-cb}$  value, calculate the WHPs' elastic  
 372 stiffness  $K_{fe}$  from Eq. (7). Moreover, to derive a relationship between the length of the  
 373 tapered part of half a WHP,  $L_{WHP}$ , and the external diameter of the WHP,  $D_e$ ,  
 374 substitute  $D_i$  from Eq. (8) into the following relationship [29,47]:

375 
$$L_{WHP} = \frac{2.566 \cdot D_e^3}{\pi \cdot D_i^2} \quad (9)$$

376 Both  $L_{WHP}$  and  $D_e$  are described in Detail 1 of Figure 3(a). A second relationship  
 377 between  $L_{WHP}$  and  $D_e$ , can be derived by substituting  $K_{fe}$  from above and  $D_i$  from Eq.  
 378 (8) into the following relationship [13,29]:

379 
$$K_{fe} = 2 \cdot \frac{9 \cdot \pi \cdot D_e^3 \cdot D_i \cdot E_{WHP} \cdot G_{WHP}}{40 \cdot E_{WHP} \cdot D_e^2 \cdot L_{WHP} + 48 \cdot G_{WHP} \cdot L_{WHP}^3} \quad (10)$$

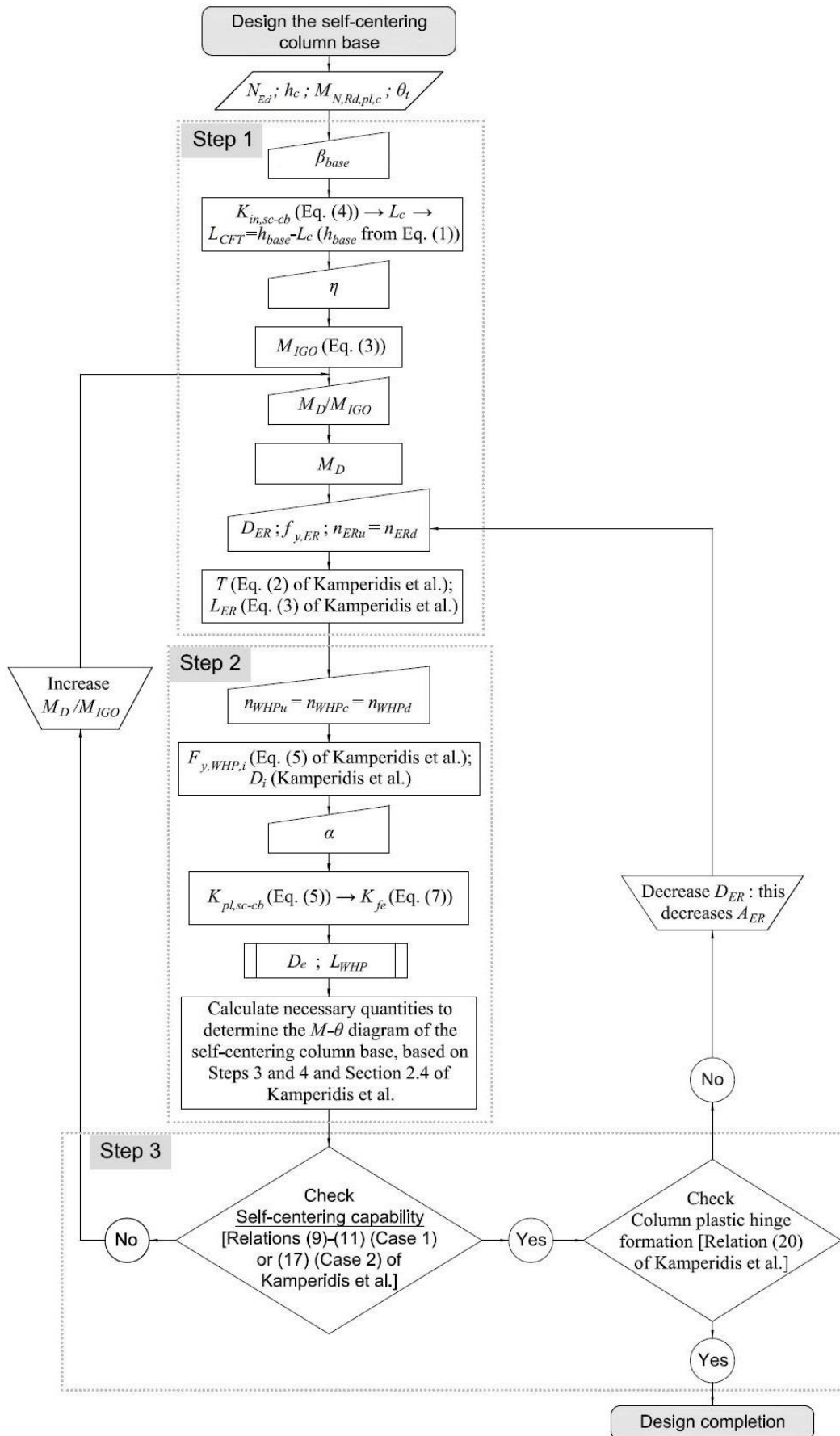
380 where  $E_{WHP}$  and  $G_{WHP}$  are the elastic and shear moduli of the WHP material. Solving  
 381 the system of Eqs. (9) and (10), the values of  $D_e$  and  $L_{WHP}$  can be derived.

382 Step 3: Check the self-centering capability of the column base and the column plastic hinge  
 383 avoidance

384 The self-centering capability of the column bases is checked by utilising Relationships (9)  
 385 through (11) and Relationship (17) from [29]. There are two cases:

386 (a) If self-centering behaviour is achieved, then proceed with checking whether a  
 387 plastic hinge is formed at the bottom of the column member. This is done by  
 388 utilising Relationship [20] of [29]. Two case are now identified:

- 389           1. A plastic hinge is formed: in this case, decrease  $A_{ER}$  in Step 1(e) by employing  
390                   a smaller tendon (smaller  $D_{ER}$ ), and repeat all steps up to this point until this check  
391                   is satisfied. Then finalize the procedure.
- 392           2. A plastic hinge is not formed: in this case, finalize the design process.
- 393       (b) If self-centering behaviour is not achieved, return to Step 1(c) and increase the ratio  
394            $M_D/M_{IGO}$ . Then, repeat the design procedure up to Step 3(a) until self-centering is  
395           achieved and plastic hinge is not formed at the column. When Step 3(a) is fully  
396           satisfied, complete the design process.
- 397       The design steps are summarized in the flowchart of Figure 4.



398  
399

Figure 4 Flowchart of the design approach of the self-centering column bases, based on the design procedure proposed in Kamperidis et al. [29].

400 3.3 Self-centering column base designs

401 Table 1 lists the normalised base structural properties of the sixteen self-centering column  
 402 base designs and Table 2 presents their key design characteristics. These design  
 403 characteristics were derived utilising the design procedure presented in Section 3.2. The  
 404 notation utilised in Table 2 is described in Figure 3(a) (and its Detail 1) and in Section 3.2.

405 Table 1. Normalised base structural properties of the sixteen self-centering column bases.

Frame	$\eta$	$\beta_{base}$ (%)	$\alpha$ (%)
H40K133A5	0.4	133	5
H40K133A15	0.4	133	15
H40K167A15	0.4	167	15
H40K167A5	0.4	167	5
H40K133A10	0.4	133	10
H40K167A10	0.4	167	10
H40K133A24	0.4	133	24.5
H35K133A5	0.35	133	5
H35K133A15	0.35	133	15
H35K167A15	0.35	167	15
H35K167A5	0.35	167	5
H35K133A10	0.35	133	10
H35K167A10	0.35	167	10
H35K200A10	0.35	200	10
H35K133A20	0.35	133	20
H30K133A10	0.30	133	10

406

407 Table 2. Key column base design characteristics of the sixteen SC-MRF-CBs.

Frame	$L_{WHP}$ (m)	$D_e$ (m)	$D_i$ (m)	$F_{y,WHP,i}$ (kN)	$K_{fe}$ (MN/m)	$L_{sp}$ (m)	$h_{wp}$ (m)	$L_{ER}$ (m)	$D_{ER}$ (m)	$z_d$ (m)	$z_{ER,d}$ (m)	$L_{CFT}$ (m)	$T$ (kN)
H40K133A5	0.12	0.04	0.02	161.78	109.22	0.37	0.24	7.49	0.02	0.24	0.09	0.44	262.70
H40K133A15	0.07	0.03	0.02	156.39	260.19	0.33	0.21	7.47	0.02	0.26	0.16	0.44	271.41
H40K167A15	0.06	0.03	0.02	158.54	307.41	0.33	0.20	7.39	0.02	0.24	0.37	0.73	273.25
H40K167A5	0.21	0.05	0.02	151.38	38.68	0.40	0.27	9.59	0.02	0.25	0.38	0.73	228.89
H40K133A10	0.06	0.04	0.02	166.28	357.10	0.33	0.20	8.50	0.02	0.21	0.15	0.44	274.02
H40K167A10	0.10	0.04	0.02	132.46	122.24	0.34	0.22	7.62	0.02	0.42	0.37	0.73	261.05
H40K133A24	0.06	0.03	0.02	163.63	396.73	0.32	0.20	5.52	0.03	0.19	0.10	0.44	281.83
H35K133A5	0.12	0.04	0.02	136.90	89.09	0.36	0.23	7.58	0.02	0.27	0.12	0.44	204.77
H35K133A15	0.06	0.04	0.02	142.89	264.52	0.32	0.20	6.64	0.02	0.22	0.16	0.44	212.16
H35K167A15	0.06	0.03	0.02	100.44	189.61	0.30	0.18	7.32	0.02	0.56	0.36	0.73	212.51
H35K167A5	0.19	0.04	0.02	125.10	34.27	0.38	0.26	8.73	0.02	0.27	0.38	0.73	171.44
H35K133A10	0.08	0.04	0.02	142.58	184.52	0.34	0.21	6.35	0.02	0.23	0.16	0.44	207.34
H35K167A10	0.05	0.04	0.02	88.76	184.92	0.30	0.17	8.65	0.02	0.70	0.36	0.73	215.25
H35K200A10	0.06	0.04	0.02	125.24	251.67	0.31	0.19	8.70	0.02	0.34	0.50	0.91	212.51
H35K133A20	0.06	0.03	0.02	113.55	252.32	0.31	0.18	7.64	0.03	0.44	0.13	0.44	212.51
H30K133A10	0.06	0.03	0.02	104.64	212.41	0.30	0.18	5.99	0.03	0.37	0.15	0.44	151.00

408

#### 409 4 NON-LINEAR MODELS

410 The OpenSees platform [48] was used to model the prototype SC-MRF and SC-MRF-CBs.  
411 The PT beam-column connections in all frames were modelled as in [35]. The columns and  
412 the length of the beams that is reinforced were modelled with beam-column fiber elements  
413 that exhibit bi-linear elastoplastic stress-strain behaviour. Force-based beam-column fiber  
414 elements with end hinges [49] were used for the un-reinforced lengths of the beams. The  
415 stress-strain cyclic behaviour of the fibers was modelled by utilising the modified Ibarra-  
416 Krawinkler model [50]. This model was used because it captures the strength and stiffness  
417 degradation resulting from beam local buckling observed after the end of the beam flange  
418 reinforcing plates. This type of modelling was used in [51] and results in hysteretic curves for  
419 flexural members that are smooth and similar to the ones observed in experiments. The  
420 Ibarra-Krawinkler model does not take into account the effect of a variable axial force on the  
421 bending deterioration parameters [51]. The use of fiber elements results in reductions of the  
422 bending strength of the beam-column elements due to the variable axial-moment interaction  
423 [51]. Thus, this approach also captures the axial force (caused by the PT force at the tendons)  
424 – bending moment interaction in the beams of the frames [35,51]. Panel zones are modelled  
425 based on [52]. The OpenSees model developed in [29] is used for the column bases of the  
426 SC-MRF-CBs. The gravity columns of the tributary area of the frames are modelled as three  
427 lean-on columns to take into account P- $\Delta$  effects. Truss elements that connect the nodes of  
428 the lean-on columns to nodes defined along the length of the beams at the points where the  
429 secondary beams are placed are used to model diaphragm action of the composite slabs. The  
430 diaphragm also helps to avoid the shortening of the PT beams (as these are seen in Figure  
431 2(a)) due to the increase of the post-tensioning forces caused by to the connections' gap  
432 opening and closing during seismic loads (the PT beams are only resist the constant axial  
433 force caused by the initial post-tensioning of their PT bars [10]). The stiffness of these trusses

434 is 100 times larger than that of the axial stiffness of the beam. By connecting separately each  
 435 bay's secondary beam nodes with the corresponding lean-on column node of the same storey,  
 436 these stiff truss elements help to model the discontinuity between the composite slabs that  
 437 correspond to each different bay of the self-centering system, as per the tributary area of the  
 438 bay. Discontinuity between the composite slab and the flanges of the columns of the self-  
 439 centering system is also assumed for the floor system utilised in this work [53]. The aim of  
 440 the above floor system discontinuities is to avoid that the PT beam be restrained by the  
 441 composite slab (minimizing the damage in the slab also); allow the free gap opening and  
 442 closing of the PT connection (thus, not affecting the connection's hysteretic behaviour)  
 443 [10,53]; and allow for the unobstructed self-centering frame expansion [10,36]. More details  
 444 on the adopted floor system can be found in [10,53,54]. The tendons of the column bases  
 445 were modelled to fracture to more accurately simulate the actual collapse limit of the frames  
 446 under investigation. To this purpose, the Fatigue material of OpenSees [48] was utilised in  
 447 conjunction with the parent material of the tendons. The parent material of the tendons is the  
 448 material around which the Fatigue material is wrapped [48], and which in this case is the  
 449 material steel01 of OpenSees [48]. The material steel01 has a bilinear elastoplastic hysteresis  
 450 with post-stiffness ratio equal to 0.03 [29]. The Fatigue material is wrapped around the  
 451 steel01 material without altering the stress-strain relationship of the latter [48]. The Fatigue  
 452 material utilises the Coffin-Manson relationship [55] and the Palmgren-Miner linear damage  
 453 accumulation rule [55] to model their low-cycle fatigue and fracture. The Coffin-Manson rule  
 454 is expressed by the relationship:

$$455 \quad \frac{\Delta \varepsilon_p}{2} = \varepsilon_f' \cdot (2 \cdot N_f)^m \quad (11)$$

456 where  $\frac{\Delta \varepsilon_p}{2}$  is the plastic strain amplitude;  $\varepsilon_f'$  the fatigue ductility coefficient, which represents  
 457 the intersect of the plastic asymptotic line of the Coffin-Manson curve in the log-log space,

458 i.e., the strain at which one cycle will cause failure (fracture) [55,56];  $N_f$  the number of the  
459 full cycles to failure (or  $2 \cdot N_f$  the number of load reversals to failure); and  $m$  the fatigue  
460 ductility exponent, which represents the sensitivity of the log of the strain amplitude to the  
461 log of  $N_f$  [56], i.e., the slope of the Coffin-Manson curve in the log-log space. For the Fatigue  
462 material of the tendons,  $\varepsilon'_f$  was taken equal to 4%. This strain value is a conservative fracture  
463 value as: (a) it represents the initial wire fracture of the strands of the tendons, ignoring the  
464 appreciable strength reserve that remains at the tendons afterwards and through the fracture  
465 of all their wires [38,39]; (b) it considers the premature fracture of the tendons due to  
466 excessive stress concentration at the vicinity of their anchors, as per the work of Bruce and  
467 Eatherton [38], where the fracture value in question represents the average observed first-  
468 wire fracture limit (not the relevant proposed design limit) from their tested specimens,  
469 considering both the tendon materials used therein, and also a newer multiple-use barrel and  
470 wedge anchorage system that allowed for larger inelastic strains prior to initial wire fracture,  
471 compared to the traditional barrel and wedge anchorage system that the authors also tested in  
472 their work; (c) it represents the upper first-wire fracture limit attained from the tested  
473 specimens in the work of Sideris et al. [39], given that their observed strain fracture values  
474 ranged from 1.5% to 4%; and (d) it is a value much smaller than those provided by these  
475 tendons manufacturers, i.e., 6-7% [57]. The fatigue ductility exponent,  $m$ , for the Fatigue  
476 material of OpenSees, was taken equal to -0.458, as per the work of Uriz [56]. For the  
477 maximum values of strain to be set out in the model of the material, the suggested minimum  
478 and maximum values of  $-1e16$  and  $1e16$ , respectively, have been adopted [48]. To  
479 accumulate damage in the material due to the random strain amplitude excursions during an  
480 earthquake, the Fatigue material of OpenSees utilises a rainflow method [55] counting  
481 algorithm to count the number of cycles at various strain amplitudes, in conjunction with the



482 Palmgren-Miner's linear damage accumulation Rule [55]. The Palmgren-Miner's Rule is  
483 expressed by the damage index,  $D$ , which is given by the following mathematical formula:

$$484 \quad D = \sum_{i=1}^j \frac{n_i}{N_{f,i}} \quad (12)$$

485 where  $N_{f,i}$  is the number of cycles that can be resisted by the material until failure at the  $i$ th  
486 constant strain amplitude loading, in a total of  $j$  such loadings with constant strain  
487 amplitudes; and  $n_i$  is the number of loading cycles the material has undergone at the  $i$ th  
488 constant strain amplitude loading [55]. Once index  $D$  in the Fatigue material reaches the  
489 value of 1.0, the force (or stress) in the parent material becomes zero, signalling the failure of  
490 the parent material [48].

491 The fracture of the WHPs was not modelled in this study, as, based on previous experimental  
492 and numerical studies [14,54,58], their geometry and position around the column bases can  
493 be selected to avoid fracture before the building's seismic collapse due to second order  
494 effects [51].

## 495 **5 NON-LINEAR DYNAMIC ANALYSES**

496 The set of the far-fault ground motions of FEMA P695 [59] was used for the non-linear  
497 dynamic analyses of this study. This set comprises 22 record pairs, each with two horizontal  
498 components for a total of 44 records. The ground motions of the above set were recorded on  
499 stiff soil and at sites with distance larger than or equal to 10 km from fault rupture. The  
500 magnitudes of the earthquakes range from  $M$  6.5 to  $M$  7.6 with an average magnitude of  $M$   
501 7.0. The records were scaled to DBE and MCE, using as intensity measure (IM) the 5%  
502 spectral acceleration at fundamental period  $T_1$  of the frame models,  $S_a(T_1)$ .

### 503 *5.1 Assessment of the seismic performance of the frames*

504 The results of the 44 non-linear dynamic analyses for the SC-MRF and sixteen SC-MRF-CBs  
505 were post-processed and the median maximum values of  $\theta_{s,\max}$  of all the storeys and peak

506 floor acceleration (PFA) from all the floors are shown in Table 3. The results in Table 3  
507 indicate that the  $\theta_{s,max}$  of all SC-MRF-CBs is lower than that of the SC-MRF under the FOE,  
508 DBE and MCE seismic intensity levels. In particular, for the FOE intensity level, the relative  
509 reduction of the  $\theta_{s,max}$  of the SC-MRF-CBs compared to that of the SC-MRF ranges from  
510 3.03% for the H35K167A5 to 23.65% for the H35K167A10. Under the DBE, the relevant  
511 minimum reduction of  $\theta_{s,max}$  is 1.42% and achieved for the H35K133A5 and the maximum is  
512 24.13% and achieved for the H40K167A15. Under the MCE, the H35K133A5 achieves the  
513 minimum reduction of  $\theta_{s,max}$  equal to 0.95% and the H35K167A10 the maximum equal to  
514 18.55%. Moreover, all the SC-MRF-CBs achieve  $\theta_{s,max}$  lower than the “life safety” and  
515 “collapse prevention” limits of EC8 [6] and ASCE/SEI 41-06 [60]. As it can be seen from  
516 Table 3, the SC-MRF-CBs achieve as much as a 24.05% overall  $\theta_{s,max}$  reduction (minimum  
517 reduction between all seismic intensity levels for the H35K167A10). These results  
518 demonstrate that the new column base configuration is very effective in reducing  $\theta_{s,max}$ , and  
519 that is done by only adjusting its base stiffness and strength characteristics.

520 Table 3. Median maximum values of  $\theta_{s,max}$  of all the storeys and PFA from all the floors of the  
521 SC-MRF and SC-MRF-CB design cases.

Frame	Fundamental Period $T_1$ (s)	$\theta_{s,max}$ (%)			PFA (g)		
		FOE	DBE	MCE	FOE	DBE	MCE
SC-MRF	0.94	0.655	1.814	2.623	0.499	1.043	1.487
H40K133A5	0.95	0.547	1.667	2.416	0.506	0.980	1.481
H40K133A15	0.95	0.530	1.529	2.336	0.534	0.932	1.385
H40K167A15	0.93	0.519	1.376	2.170	0.521	0.932	1.362
H40K167A5	0.93	0.621	1.671	2.494	0.520	1.036	1.462
H40K133A10	0.95	0.530	1.510	2.319	0.526	0.918	1.356
H40K167A10	0.93	0.531	1.433	2.264	0.542	0.954	1.316
H40K133A24	0.95	0.530	1.448	2.294	0.519	0.919	1.508
H35K133A5	0.95	0.576	1.788	2.598	0.509	0.911	1.428
H35K133A15	0.95	0.542	1.655	2.353	0.506	0.918	1.341
H35K167A15	0.93	0.501	1.384	2.147	0.489	0.903	1.416
H35K167A5	0.93	0.635	1.745	2.538	0.556	0.966	1.418
H35K133A10	0.95	0.546	1.683	2.379	0.495	0.910	1.392
H35K167A10	0.93	0.500	1.396	2.136	0.494	0.899	1.400
H35K200A10	0.91	0.506	1.534	2.140	0.504	0.887	1.367
H35K133A20	0.95	0.522	1.542	2.299	0.515	0.914	1.364
H30K133A10	0.95	0.543	1.667	2.299	0.470	0.864	1.364

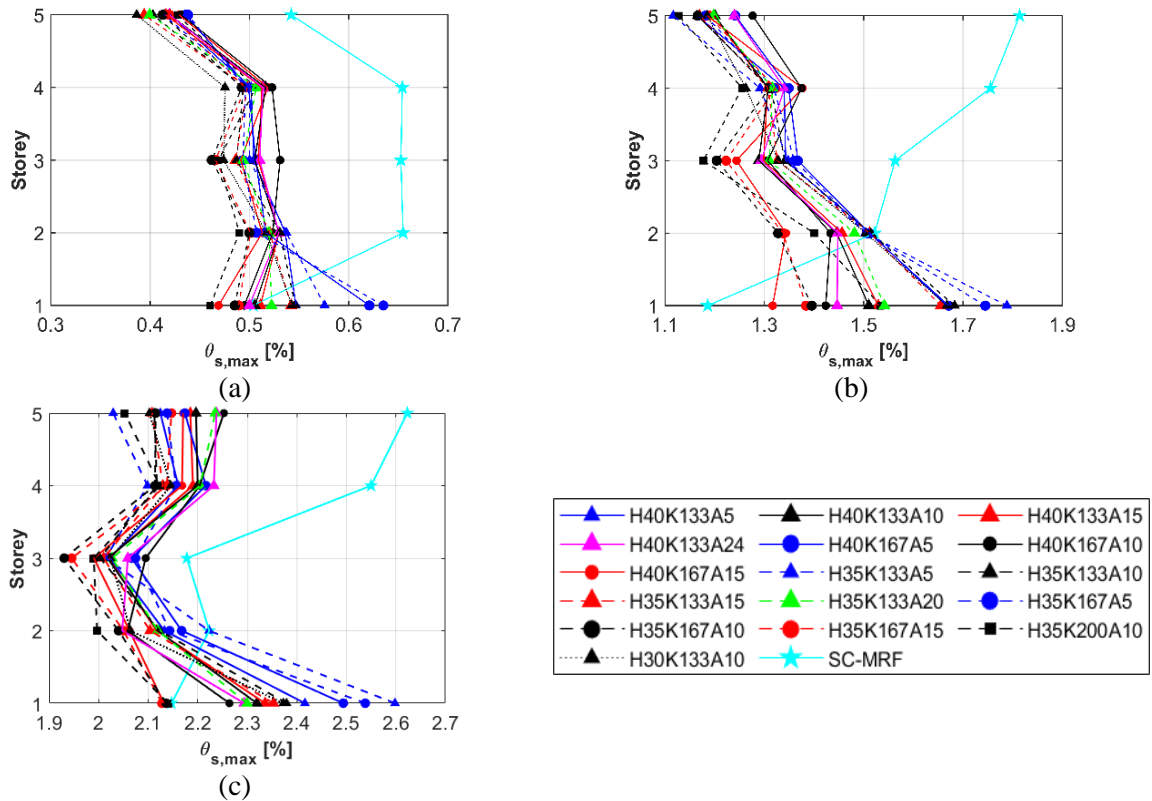
522

523 The maximum values of PFA from all the floors of all the SC-MRF-CBs are lower than that  
524 of the SC-MRF under the DBE. Under the FOE and MCE, all the values of PFA of the SC-  
525 MRF-CBs are lower than that of the SC-MRF, with the exception of H35K167A5 and  
526 H40K133A24 for the FOE and MCE, respectively. The PFA reduction observed in the SC-  
527 MRF-CBs ranges from 5.81% to 23.65%, from 0.73% to 17.19% and from 0.42% to 11.46%,  
528 under the FOE, DBE and MCE, respectively. Thus, the new self-centering column bases can  
529 be very effective in reducing the PFA of an SC-MRF that will be equipped with these column  
530 bases.

531 These results show that the SC-MRF-CBs have in general better seismic performance than  
532 the SC-MRF in terms of the above two engineering demand parameters examined. Low  
533 values of  $\theta_{s,max}$  and PFA are associated with low non-structural and equipment damage. Thus,  
534 non-structural elements and equipment installed to SC-MRF-CBs may exhibit less damage.  
535 In addition, since  $\theta_{s,max}$  dictates the design of columns in the serviceability limit state, there is  
536 a potential of reducing the cross-sections of the members of the SC-MRF-CBs because they  
537 exhibit very low values of  $\theta_{s,max}$ .

538 Figure 5 depicts the comparison of the height-wise distribution of  $\theta_{s,max}$ , of all the frames  
539 studied herein under the FOE, DBE and MCE. Under the FOE, the H40K167A15,  
540 H40K167A10, H40K133A24, H35K167A15, H35K167A10 and H35K200A10 have lower  
541 values of  $\theta_{s,max}$ , for all the storeys. The rest of the SC-MRF-CBs have lower values of  $\theta_{s,max}$ ,  
542 for all the storeys, with the exception of the first storey. It is also observed that the SC-MRF-  
543 CBs have lower values of  $\theta_{s,max}$ , for all the storeys, with the exception of the first storey under  
544 the DBE level. The same trend is observed for all the frames at the MCE level, with the  
545 exception of H35K200A10, H35K167A15, H35A167A10 and H40K167A15, which have  
546 lower values of  $\theta_{s,max}$  for all the storeys. The reason for the increased first-storey  $\theta_{s,max}$

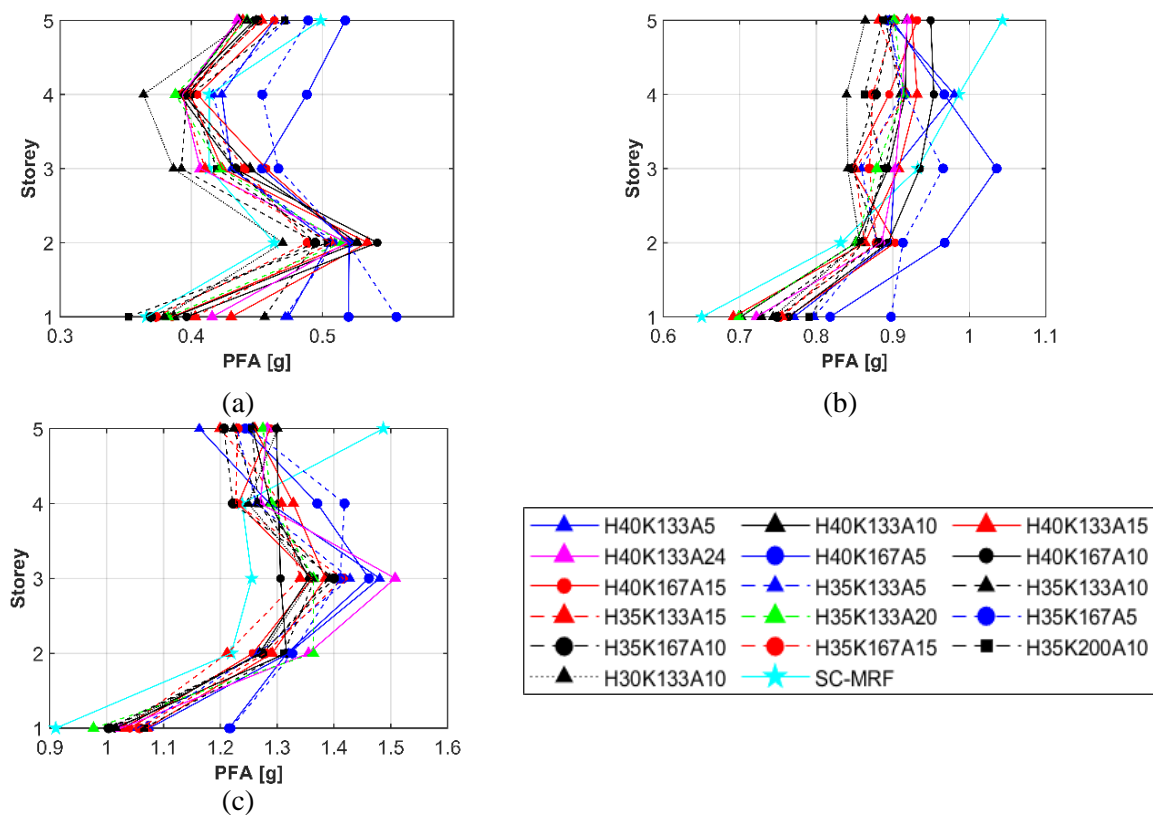
547 demands of most of the SC-MRF-CBs is attributed to the gap openings of their self-centering  
 548 column bases.



549 Figure 5 Comparison of the median height-wise distribution of the  $\theta_{s,max}$  of the SC-MRF and  
 550 SC-MRF-CB designs under the: (a) FOE; (b) DBE; and (c) MCE intensity levels.  
 551

552 Figure 6 shows the comparison of the height-wise distribution of PFA under the FOE, DBE  
 553 and MCE. Under the FOE, apart from the H35K200A10, all the other SC-MRF-CBs have  
 554 higher PFAs compared to that of the SC-MRF. In the second storey, all the SC-MRF-CBs  
 555 have higher PFAs compared to that of the SAC-MRF. In the third storey, there is a shift in  
 556 this trend; H30K133A10, H35K133A10, H40K133A24 and H35K133A15 have lower PFAs  
 557 than that of the SC-MRF. In the fourth storey, only H35K133A5, H40K133A5, H35K167A5  
 558 and H40K167A5 have higher PFAs than that of the SC-MRF. Finally, in the fifth storey,  
 559 apart from H40K167A5, all the other SC-MRF-CBs have lower PFAs compared to that of the  
 560 SC-MRF. Under the DBE, the SC-MRF has PFAs lower than those of all the SC-MRF-CBs  
 561 in both the first and second storey. However, in the third storey, apart from H35K167A4 and  
 562 H40K176A5 which have higher PFAs, and H40K167A10 which has similar PFA, all the

563 other SC-MRF-CBs have lower PFAs compared to that of the SC-MRF. Finally, in both the  
 564 fourth and fifth storeys, all the SC-MRF-CBs have lower PFAs compared to that of the SC-  
 565 MRF. Under the MCE, apart from H35K133A15 that has lower PFA in its second storey, all  
 566 the other SC-MRF-CBs have higher PFAs in all their three first storeys as compared to those  
 567 of the SC-MRF. In the fourth storey, H40K167A15, H35K167A10 and H35K167A15 have  
 568 lower PFAs as compared to the SC-MRF. Lastly, in the fifth storey, all the SC-MRF-CBs  
 569 have lower PFAs compared to that of the SC-MRF.



570 Figure 6 Comparison of the median height-wise distribution of the PFA of the SC-MRF and SC-  
 571 MRF-CBs under the: (a) FOE; (b) DBE; and (c) MCE intensity levels.

572  
 573 The PFA distribution of Figure 6 can be explained by recent studies in self-centering MRFs  
 574 with connections similar to those of the SC-MRF-CBs. These suggest that the magnitudes of  
 575 the PFAs and their distribution is influenced by the interactions between the beams and  
 576 columns of these systems. These member interactions are due to the discontinuity of their

577 connections and the asymmetry in member restraints due to the presence of the rocking in the  
578 column bases [61].

## 579 5.2 *Effect of base strength and stiffness on the seismic performance of the frames*

580 In this section, the effect of base strength and stiffness on the seismic performance of the  
581 frames examined herein is evaluated in terms of  $\theta_{s,max}$  and PFA. The parameters  $\eta$ ,  $\beta_{base}$  and  
582  $\alpha$ , that are associated with the base strength and stiffness of the frames, were used for this  
583 evaluation.

584 In order to evaluate the effect of base strength of the frames to the response parameters  $\theta_{s,max}$   
585 and PFA, the parameter  $\eta$  is examined. Thus, the design cases H40K133A10, H35K133A10  
586 and H30K133A10, with  $\eta$  equals 0.40, 0.35 and 0.30, respectively, were compared. Figures  
587 7(a) and 7(b) show  $\theta_{s,max}$  and PFA versus  $\eta$ , respectively, for the three seismic intensities  
588 examined. As indicated in Figure 7(a), when  $\eta$  increases from 0.30 to 0.35,  $\theta_{s,max}$  also  
589 increases for all the seismic intensity levels. The increase observed is 0.65%, 0.93% and  
590 3.36% under the FOE, DBE and MCE, respectively. A further increase of  $\eta$  to 0.40 results in  
591 a reduction of  $\theta_{s,max}$  for all the seismic intensity levels. The reduction of  $\theta_{s,max}$  is 2.98%,  
592 10.27% and 2.52% under the FOE, DBE and MCE, respectively. The same trend is observed  
593 for the PFA but only for the MCE intensity level. Under FOE and DBE, an increase of  $\eta$   
594 results in an increase of PFA. More specifically, when  $\eta$  increases from 0.30 to 0.35, PFA  
595 values increase by 5.07% and 5.02%, under the FOE and DBE, respectively. A further  
596 increase of  $\eta$  to 0.40 results in an increase of PFA equal to 6% and 0.94%, under the FOE and  
597 DBE, respectively.

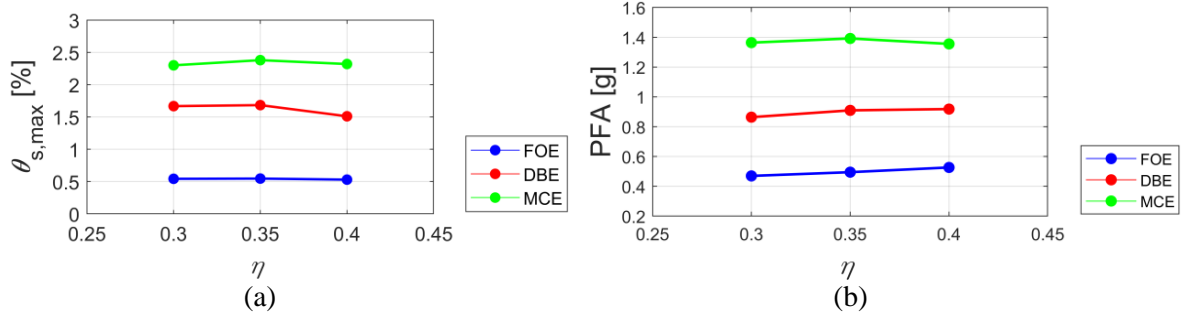


Figure 7 Effect of  $\eta$  to (a)  $\theta_{s,max}$ ; and (b) PFA.

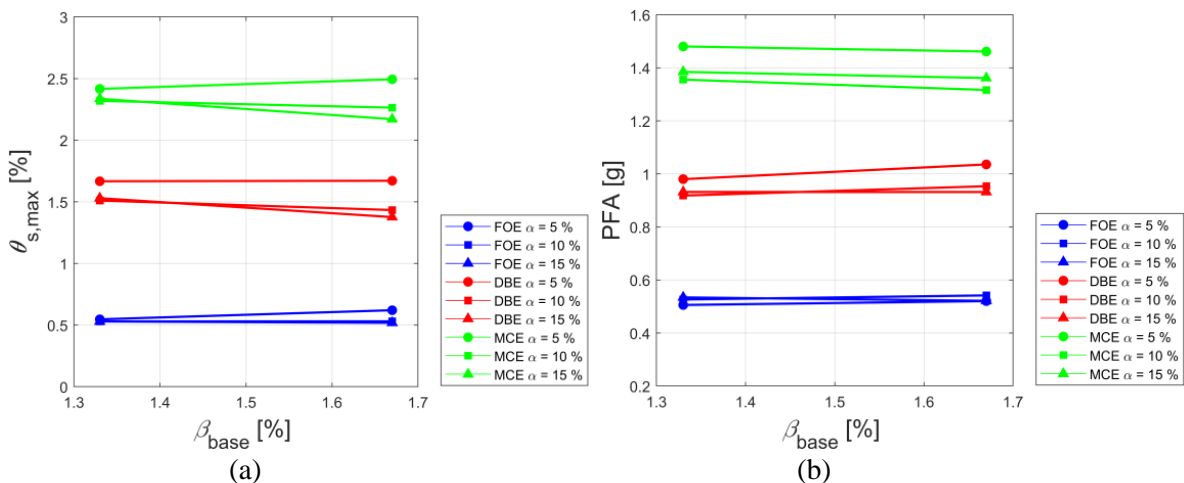
598  
599  
600  
601

602 The design cases examined herein were compared in terms of the parameters  $\beta_{base}$  and  $\alpha$  to  
603 evaluate the effect of base stiffness on their seismic response. For the frames with  $\eta=0.40$ , the  
604 following design cases were compared to evaluate the effect of  $\beta_{base}$ , i.e.: H40K133A5  
605 ( $\beta_{base}=133\%$ ) and H40K167A5 ( $\beta_{base}=167\%$ ), which have a value of  $\alpha=5\%$ ; H40K133A10  
606 ( $\beta_{base}=133\%$ ) and H40K167A10 ( $\beta_{base}=167\%$ ), with  $\alpha = 10\%$ ; and H40K133A15  
607 ( $\beta_{base}=133\%$ ) and H40K167A15, with  $\alpha=15\%$ . For the frames with  $\eta=0.35$ , the following  
608 frames were compared: H35K133A5 ( $\beta_{base}=133\%$ ) and H35K167A5 ( $\beta_{base}=167\%$ ), with  
609  $\alpha=5\%$ ; H35K133A10 ( $\beta_{base}=133\%$ ), H35K167A10 ( $\beta_{base}=167\%$ ) and H35K200A10  
610 ( $\beta_{base}=200\%$ ), with  $\alpha=10\%$ ; and H35K133A15 ( $\beta_{base}=133\%$ ) and H35K167A15 ( $\beta_{base}=167\%$ ),  
611 with  $\alpha=15\%$ . Figure 8 shows the effect of  $\beta_{base}$  to the seismic response, in terms of the  $\theta_{s,max}$   
612 and PFA, of the aforementioned design cases.

613 For the frames with  $\eta=0.40$  and  $\alpha=5\%$ , the results in Table 3 show that an increase of  $\beta_{base}$   
614 from 133% to 167% results to higher values of  $\theta_{s,max}$ , for all the intensity levels. Thus, the  
615 increase of  $\theta_{s,max}$  observed, due to the increase of  $\beta_{base}$ , is 11.91%, 0.25% and 3.11%, for the  
616 FOE, DBE and MCE seismic intensity levels, respectively. The same increase of  $\beta_{base}$ , leads  
617 to a reduction of  $\theta_{s,max}$  for all the seismic intensity levels for the frames with  $\eta=0.40$  and  
618  $\alpha=10\%$ . The reduction observed equals 2.09%, 10.01% and 7.09%, under the FOE, DBE and  
619 MCE, respectively. Finally, an increase of  $\beta_{base}$  from 133% to 167% results to lower  $\theta_{s,max}$  for  
620 the frames with  $\eta=0.40$  and  $\alpha=15\%$ , under the DBE and MCE. This trend is reversed under  
621 the FOE. In addition, the increase of  $\beta_{base}$  from 133% to 167 results to higher values of PFA

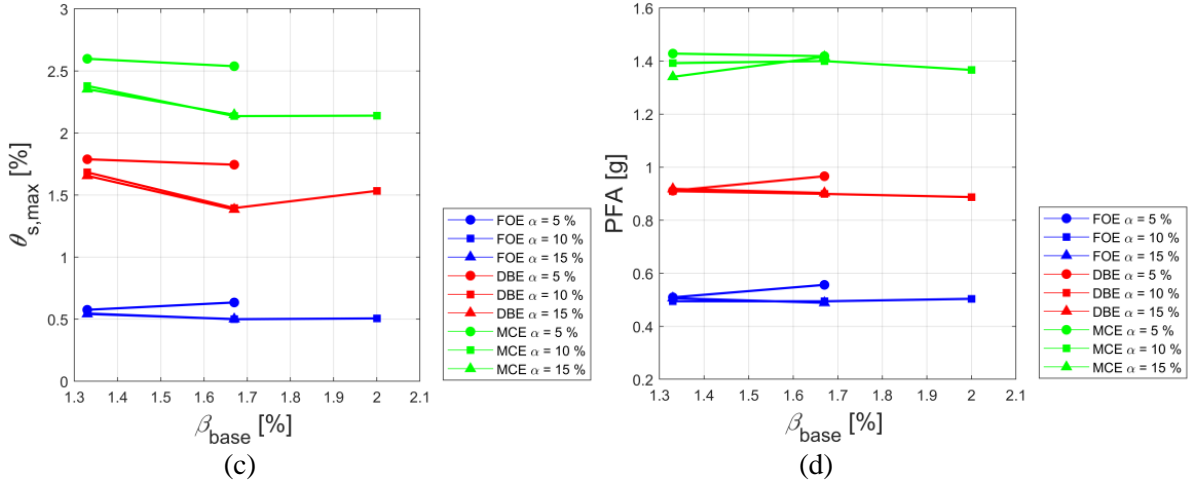
622 under the FOE and DBE, for the frames with  $\eta=0.40$  and  $\alpha=5\%$  and  $\alpha=10\%$ . In contrary, the  
 623 same increase of  $\beta_{base}$  leads to a reduction of PFA under all the seismic intensity levels for the  
 624 frames with  $\eta=0.40$  and  $\alpha=15\%$ .

625 For the frames with  $\eta=0.35$  and  $\alpha=10\%$  and  $\alpha=15\%$ , results in Table 3 show that an increase  
 626 of  $\beta_{base}$  from 133% to 167% results to lower values of  $\theta_{s,max}$ , for all the seismic intensity  
 627 levels. For the frames with  $\alpha=10\%$ , the reduction of  $\theta_{s,max}$ , due to the increase of  $\beta_{base}$ , is  
 628 8.46%, 17.09% and 10.21%, under the FOE, DBE and MCE, respectively. For the frames  
 629 with  $\alpha=10\%$ , this reduction equals 7.56%, 16.40% and 8.76% under the FOE, DBE and  
 630 MCE. In the frames with  $\eta=0.35$  and  $\alpha=5\%$ , an increase of  $\beta_{base}$  from 133% to 167% results  
 631 to 2.43% and 2.31% lower values of  $\theta_{s,max}$ , under the DBE and MCE, respectively. An  
 632 opposite trend is observed under the FOE. For the frames with  $\eta=0.35$  and  $\alpha=5\%$ , results  
 633 show that an increase of  $\beta_{base}$  from 133% to 167% results to 8.46% and 5.63% higher values  
 634 of PFA under the FOE and DBE, respectively. Under the MCE, the PFA of the frame with  
 635  $\beta_{base}=133\%$  is 0.68% larger than that of with  $\beta_{base}=167\%$ . For the frames with  $\eta=0.35$  and  
 636  $\alpha=10\%$ , results show that an increase of  $\beta_{base}$  from 133% to 167% results to 0.08% and 1.14%  
 637 lower values of PFA under the FOE and DBE, respectively. Under the MCE, the PFA of the  
 638 frame with  $\beta_{base}=167\%$  is 0.56% larger than that of with  $\beta_{base}=133\%$ . A similar trend is  
 639 observed for the frames with  $\eta=0.35$  and  $\alpha=15\%$ .



640  
641





642  
643  
644  
645  
646

Figure 8 Effect of  $\beta_{base}$  to (a)  $\theta_{s,max}$  ( $\eta = 0.40$ ); (b) PFA ( $\eta = 0.40$ ); (c)  $\theta_{s,max}$  ( $\eta = 0.35$ ); and (d) (b) PFA ( $\eta = 0.35$ ).

647

For the design cases with  $\eta=0.40$ , the following frames were compared to evaluate the effect

648

of  $\alpha$  on  $\theta_{s,max}$  and PFA: H40K133A5 ( $\alpha=5\%$ ), H40K133A10 ( $\alpha=10\%$ ), H40K133A15

649

( $\alpha=15\%$ ) and H40K133A24 ( $\alpha=24.5\%$ ), with  $\beta_{base}=133\%$ ; and H40K167A5 ( $\alpha=5\%$ ),

650

H40K167A10 ( $\alpha=10\%$ ) and H40K167A15 ( $\alpha=15\%$ ), with  $\beta_{base}=167\%$ . This effect is shown

651

in Figures 9(a)-(d) for these design cases. It is observed that the highest value of  $\theta_{s,max}$  is

652

achieved by H40K133A5 ( $\alpha=5\%$ ) for the frames with  $\beta_{base}=133\%$ , under the FOE, DBE and

653

MCE. The lowest values of  $\theta_{s,max}$  are achieved for the frame H40K133A24 ( $\alpha=24.5\%$ ) for

654

both the DBE and MCE. Frame H40K133A5 with  $\alpha=5\%$  has the best PFA performance,

655

achieving the lowest value of PFA under the FOE. In addition, the frame with  $\alpha=10\%$  has the

656

best PFA performance under the DBE and MCE. For the frames with  $\beta_{base}=167\%$ , increasing

657

the value of  $\alpha$  from 5% to 10%, results in a reduction of  $\theta_{s,max}$  for all the seismic intensity

658

levels. This reduction equals 14.48%, 14.22% and 9.21%, under the FOE, DBE and MCE,

659

respectively. A further increase of  $\alpha$  from 10% to 15%, leads to a reduction of  $\theta_{s,max}$ , which

660

equals 2.31%, 3.98% and 4.23%, under the FOE, DBE and MCE, respectively. Increasing the

661

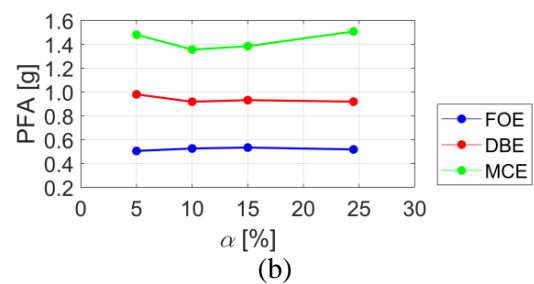
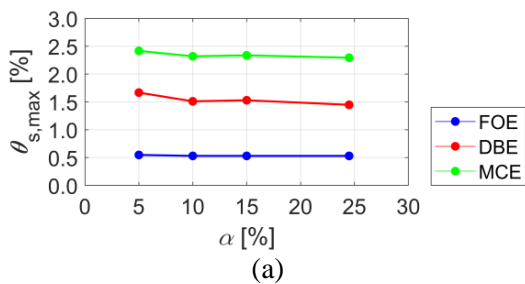
value of  $\alpha$  from 5% to 10%, leads to a 3.95% increase, and 7.94% and 9.93% reduction of

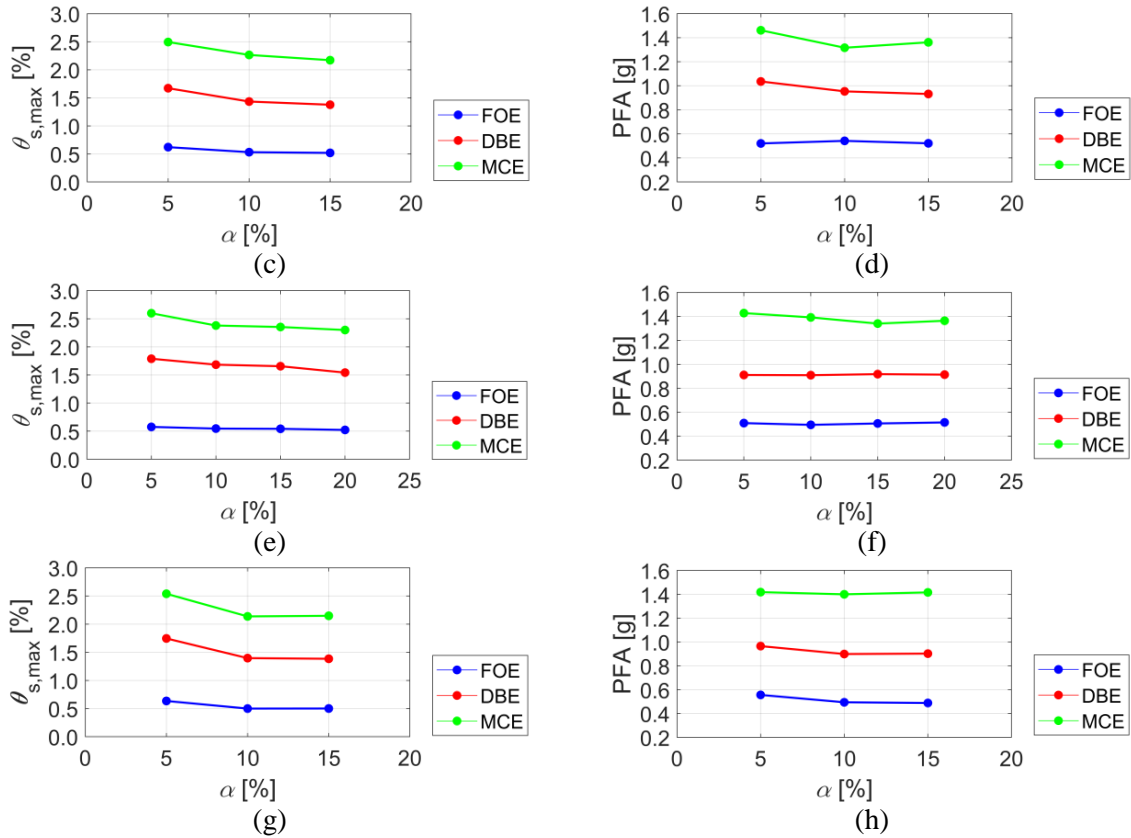
662

PFA under the FOE, DBE and MCE, respectively. Finally, a further increase of  $\alpha$  from 10%

663 to 15%, leads to a 3.76% and 2.29% reduction and 3.32% increase of PFA, under the FOE,  
 664 DBE and MCE, respectively.

665 For the design cases with  $\eta=0.35$ , the following frames were compared: H35K133A5  
 666 ( $\alpha=5\%$ ), H35K133A10 ( $\alpha=10\%$ ), H35K133A15 ( $\alpha=15\%$ ) and H35K133A20 ( $\alpha=20\%$ ), with  
 667  $\beta_{base}=133\%$ ; and H35K167A5 ( $\alpha=5\%$ ), H35K167A10 ( $\alpha=10\%$ ) and H35K167A15 ( $\alpha=15\%$ ),  
 668 with  $\beta_{base}=167\%$  (Figures 9(e)-(h)). For the frames with  $\beta_{base}=133\%$ , the lowest values of  
 669  $\theta_{s,max}$  is achieved for the frame with the higher value of  $\alpha$ , i.e., 20% (H35K133A20), for all  
 670 the seismic intensity levels. The frame with  $\alpha=5\%$  (H35K133A10) has the best PFA  
 671 performance, achieving the lowest value of PFA under DBA and MCE. In addition, the frame  
 672  $\alpha=15\%$  has the best PFA performance under the MCE. For the frames with  $\beta_{base}=167\%$ ,  
 673 increasing the value of  $\alpha$  from 5% to 10%, results in a reduction of  $\theta_{s,max}$  for all the seismic  
 674 intensity levels. This reduction equals 21.26%, 20.02% and 15.83%, under the FOE, DBE  
 675 and MCE, respectively. A further increase of  $\alpha$  from 10% to 15%, leads to a 0.23% increase,  
 676 0.83% reduction and 0.49% increase of  $\theta_{s,max}$ , under the FOE, DBE and MCE, respectively.  
 677 Increasing the value of  $\alpha$  from 5% to 10%, leads to a 11.14%, 6.89% and 1.30% reduction of  
 678 PFA under the FOE, DBE and MCE, respectively. Finally, a further increase of  $\alpha$  from 10%  
 679 to 15%, results to a 1.14% reduction, and 0.38% and 1.14% increase of PFA, under the FOE,  
 680 DBE and MCE, respectively.

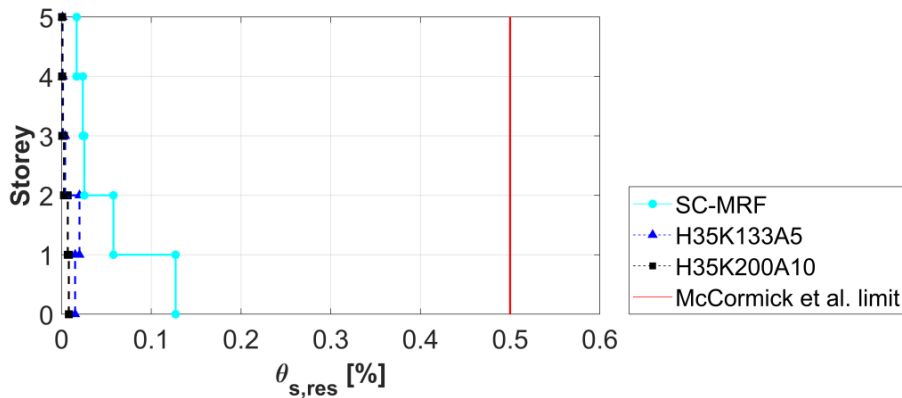




681 Figure 9 Effect of  $\alpha$  to (a)  $\theta_{s,max}$  ( $\eta = 0.40$ ,  $\beta_{base} = 133\%$ ); (b) PFA ( $\eta = 0.40$ ,  $\beta_{base} = 133\%$ ); (c)  $\theta_{s,max}$  ( $\eta$   
682  $= 0.40$ ,  $\beta_{base} = 167\%$ ); (d) PFA ( $\eta = 0.40$ ,  $\beta_{base} = 167\%$ ); (e)  $\theta_{s,max}$  ( $\eta = 0.35$ ,  $\beta_{base} = 133\%$ ); (f) PFA ( $\eta$   
683  $= 0.35$ ,  $\beta_{base} = 133\%$ ); (g)  $\theta_{s,max}$  ( $\eta = 0.35$ ,  $\beta_{base} = 167\%$ ); and (h) PFA ( $\eta = 0.35$ ,  $\beta_{base} = 167\%$ ).  
684

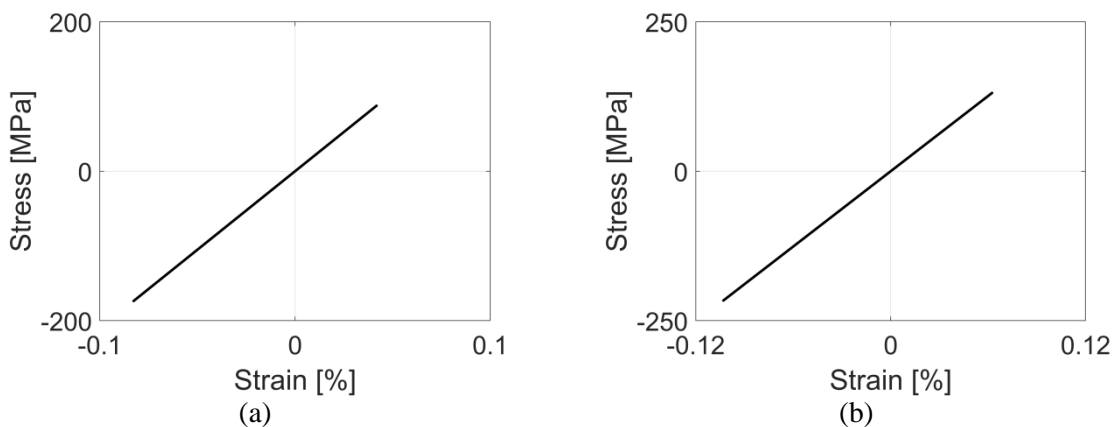
### 685 5.3 Residual drift performance of the frames

686 Figure 10 shows the height-wise distribution of the median residual drifts ( $\theta_{s,res}$ ) of the SC-  
687 MRF, H35K133A5 and H35K200A10 under the MCE, together with a maximum allowable  
688 limit for residual drifts. This limit was proposed by McCormick et al. [62] and utilised to  
689 characterise reparability in such buildings. The rationale for presenting only these two SC-  
690 MRF-CBs is that they are those that exhibit the lowest and highest  $\theta_{s,res}$  values among the  
691 investigated frames. Residual drifts are recognised as an important index of the seismic  
692 performance and resilience of structures since they are directly linked to probability of  
693 demolition of a building [34,62]. It is observed that all the frames have values of  $\theta_{s,res}$   
694 than the proposed limit in [62] and that both H35K133A5 and H35K200A10 have lower  $\theta_{s,res}$   
695 values for all their storeys than those of the SC-MRF. These values are almost negligible.



696 Figure 10 Height-wise distribution of median residual drifts of the SC-MRF, H35K133A5 and  
 697 H35K200A10 under the MCE, plotted against the maximum allowable limit for residual interstorey  
 698 drifts proposed by McCormick et al. [62].  
 699

700 Figure 11 shows the stress-strain hysteresis loops in the flanges of the first-storey columns  
 701 (Figure 3(a)) of the H35K133A5 and H35K200A10 under the 1992 Landers earthquake  
 702 scaled to the MCE. It is observed, that the two SC-MRF-CBs do not exhibit any plastic  
 703 deformation in their first-storey columns since the developed maximum stress at the extreme  
 704 fibers of their flanges is well below the yield stress limit of 355 MPa. Thus, damage is  
 705 avoided at their self-centering column bases. This shows that the values of  $\theta_{s,res}$  observed in  
 706 SC-MRF-CBs (Figure 10) mainly result from permanent deformations that occur at PT beam-  
 707 column connections. Similar results are observed for the rest of the SC-MRF-CBs and ground  
 708 motions but are not shown herein due to lack of space.



709 Figure 11 Stress strain hysteresis loops of a flange of a first storey column of: (a) H35K133A5; and  
 710 (b) H35K200A10 under the 1992 Landers earthquake scaled to MCE.  
 711

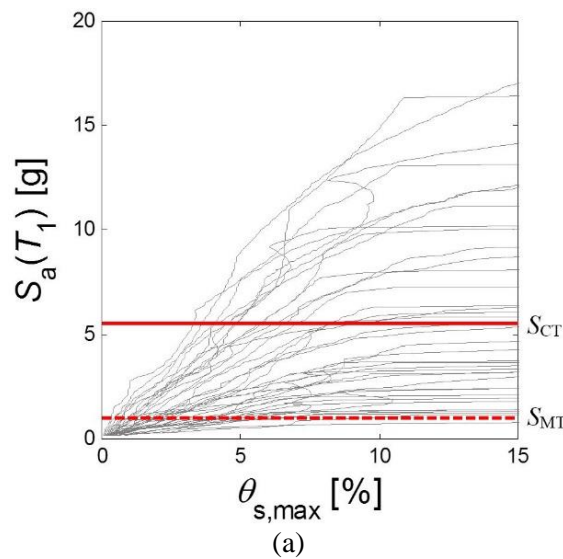
## 712 6 COLLAPSE ASSESSMENT

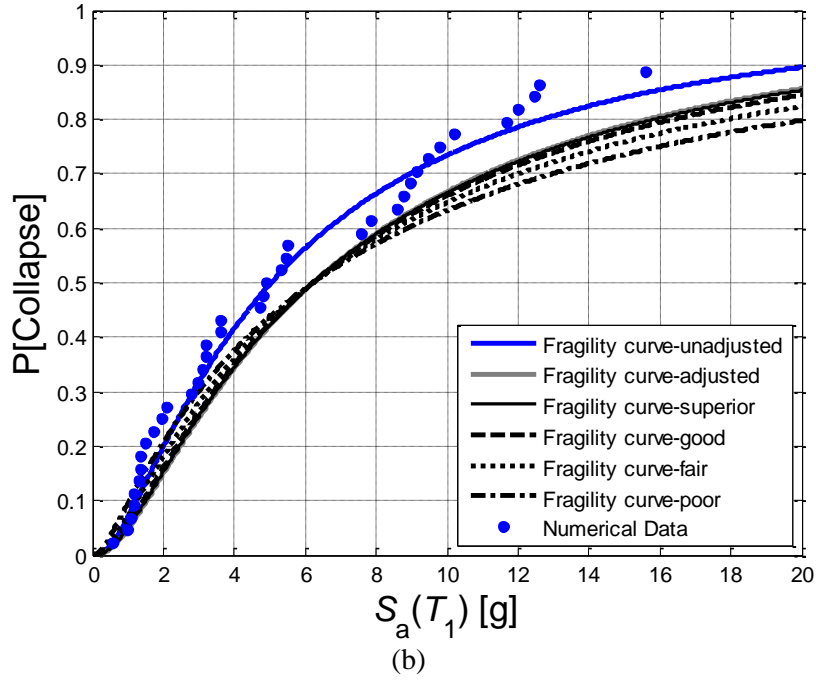
713 The collapse resistance of the frames is determined by the use of IDA [63].  $S_a(T_1)$  is the IM  
714 used herein and  $\theta_{s,max}$  was the response parameter monitored. The set of ground motions used  
715 for the non-linear dynamic analyses in Section 5 were used also for the IDAs. For each  
716 design case and ground motion, the collapse  $S_a(T_1)$  value at which  $\theta_{s,max}$  increases without  
717 bound was obtained. To determine the limit of collapse, the criterion adopted by Seo et al.  
718 [64] was used. Thus, the incremental slopes were calculated by drawing straight lines  
719 between the consecutive data points in the IDA curve. The lowest  $S_a(T_1)$  value corresponding  
720 to the  $i^{th}$  data point with the slope between the  $i^{th}$  and  $i+1^{th}$  points being less than 10% of the  
721 initial slope on the IDA curve was defined as the collapse  $S_a(T_1)$ . The initial slope was  
722 determined from the straight line from the origin of axis to the first data point of the IDA  
723 curve. A collapse fragility curve was generated by fitting a lognormal cumulative distribution  
724 function to the collapse  $S_a(T_1)$  values determined for each frame. The median value,  $S_{CT}$ , and  
725 the lognormal standard deviation,  $\beta$ , of collapse  $S_a(T_1)$  values define this distribution. The  
726 value of  $S_{CT}$  was amplified to take into account the effect of the distinct spectral shape of rare  
727 ground motions, characterised by the parameter  $\varepsilon$  [65]. In this work, the simplified  
728 methodology proposed by FEMA P695 [59] is adopted, where the influence of the spectral  
729 shape is taken into account by the use of a spectral shape factor ( $SSF$ ). Thus, the values of  $S_{CT}$   
730 of all the frames of this study were multiplied by  $SSF$  to estimate their true collapse capacity.

731 The parameter  $\beta$  affects the shape of the fragility curve and is a measure of the level of  
732 uncertainty in the analysis results. The system-level and the record-to-record uncertainty were  
733 used for the construction of the fragility curves. The FEMA P695 [59] regulations were used  
734 for the calculation of the total uncertainty, where additional system-level uncertainty were  
735 added from three categories [43]. The total uncertainty of the system,  $\beta_{Total}$ , is given by:

$$736 \quad \beta_{Total} = \sqrt{\beta_{RTR}^2 + \beta_{DR}^2 + \beta_{TD}^2 + \beta_{MDL}^2} \quad (13)$$

737 where  $\beta_{RTR}$  is the record-to-record uncertainty,  $\beta_{DR}$ ,  $\beta_{TD}$  and  $\beta_{MDL}$  are the additional  
 738 uncertainty because of the robustness of the design requirements, the accuracy of the test data  
 739 and the accuracy of the numerical model, respectively. The values of  $\beta_{RTR}$  were taken from  
 740 the results of the IDA, while values of the rest uncertainties were based on P695  
 741 recommendations [59]. Thus, the uncertainties  $\beta_{DR}$ ,  $\beta_{TD}$  and  $\beta_{MDL}$  can be subjectively  
 742 classified as ‘superior’, ‘good’, ‘fair’, or ‘poor’ [59]. The uncertainty due to the robustness of  
 743 the design requirements, accuracy of the test data and numerical model were assigned each  
 744 rating of ‘superior’, ‘good’, ‘fair’ and ‘poor’ together to construct four different collapse  
 745 fragility curves. The values of uncertainty for ‘superior’, ‘good’, ‘fair’ and ‘poor’ uncertainty  
 746 rating were 0.1, 0.2, 0.35 and 0.5, respectively. Figure 12 shows the IDA curves of the  
 747 H35K200A10 together with the collapse fragility curves, for different uncertainty ratings as  
 748 per the aforementioned procedure.





749 Figure 12 (a) IDA curves; and (b) corresponding collapse fragility curves of the H35K200A10.

750  
751 Finally, the constructed collapse fragility curves were used for the evaluation of the collapse  
752 risk of the frames through the adjusted collapse margin ratio (*ACMR*), defined as:

$$753 \quad ACMR = \frac{S_{CT}}{S_{MT}} \cdot SSF \quad (14)$$

754 where  $S_{CT}$ , is the median collapse intensity of the frames,  $S_{MT}$  is intensity demand to the  
755 MCE-level intensity.

## 756 **7 EFFECT OF BASE STRENGTH AND STIFFNESS ON THE COLLAPSE RISK** 757 **OF THE FRAMES**

758 Table 4 shows the collapse capacity results of all the investigated frames. The SC-MRF-CBs  
759 have larger value of collapse capacity and *ACMR*, compared to the SC-MRF. The maximum  
760 increase in collapse capacity and *ACMR* is achieved by the H35K200A10 compared to SC-  
761 MRF, whereas the minimum increase of these parameters is achieved by the H35K133A5.  
762 Collapse capacity and *ACMR* of the SC-MRF-CBs design cases are 25.08-33.23% and 23.02-  
763 27.95% higher, respectively, than that of the SC-MRF. Thus, there is a significant

764 improvement of the collapse capacity and *ACMR*, by adopting the self-centering column  
 765 bases and appropriately tuning their base stiffness and strength characteristics.

766 Figure 13 shows the collapse fragility curves of the SC-MRF, H35K133A5 and  
 767 H35K200A10 for different uncertainty ratings. These two SC-MRF-CBs were selected  
 768 because they achieve the lower and higher increase of *ACMR*, compared to the SC-MRF. It is  
 769 observed that the H35K133A5 and H35K200A10 are exhibiting, in general, the lowest  
 770 probabilities of collapse. This trend is inverted for low values of  $S_a(T_1)$ , for superior, good  
 771 and fair uncertainty ratings, and for poor uncertainty ratings the probabilities of collapse are  
 772 similar for all the frames.

773

Table 4. Collapse capacity results.

Frame	$S_{MT}$ (g)	$S_{CT}$ (g)	<i>CMR</i>	<i>SSF</i>	<i>ACMR</i>
SC-MRF	0.90	3.70	4.10	1.23	5.06
H40K133A5	0.93	5.04	5.44	1.23	6.72
H40K133A15	0.93	5.17	5.57	1.23	6.88
H40K167A15	0.95	5.39	5.67	1.23	6.97
H40K167A5	0.95	5.28	5.56	1.23	6.83
H40K133A10	0.93	5.19	5.60	1.23	6.92
H40K167A10	0.95	5.38	5.66	1.23	6.95
H40K133A24	0.92	5.04	5.45	1.24	6.74
H35K133A5	0.93	4.94	5.32	1.23	6.57
H35K133A15	0.93	5.18	5.59	1.23	6.87
H35K167A15	0.95	5.32	5.60	1.23	6.89
H35K167A5	0.95	5.27	5.54	1.23	6.80
H35K133A10	0.93	5.19	5.60	1.23	6.91
H35K167A10	0.95	5.35	5.64	1.23	6.92
H35K200A10	0.97	5.54	5.74	1.22	7.02
H35K133A20	0.93	5.04	5.43	1.23	6.70
H30K133A10	0.93	5.11	5.51	1.23	6.81

774

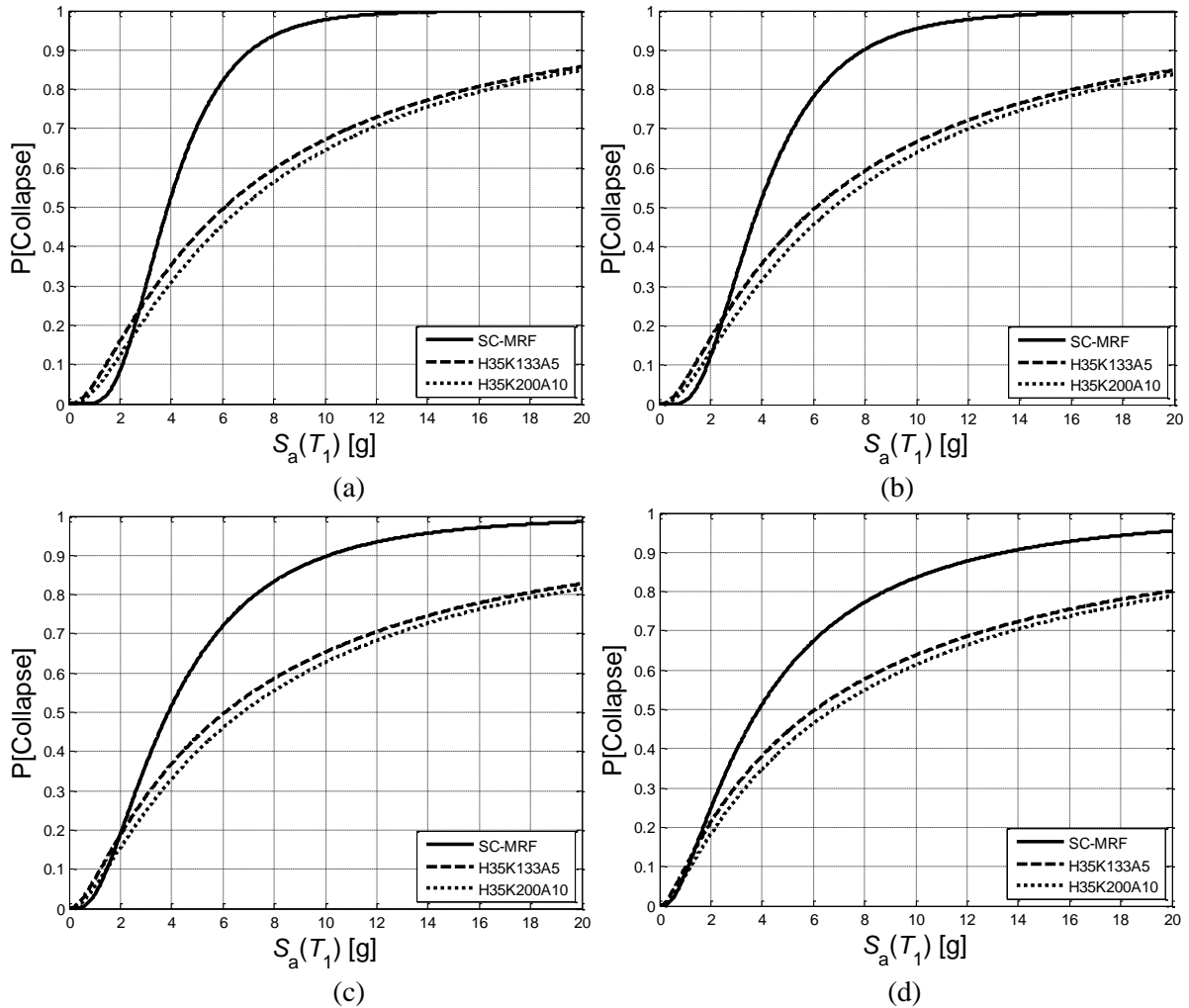
775 To evaluate the effect of base strength on the collapse risk of the frames, the base strength  
 776 factor  $\eta$  was utilised. To this end, the design cases H40K133A10, H35K133A10 and  
 777 H30K133A10, with  $\eta$  equals 0.40, 0.35 and 0.30, respectively, were compared. The  
 778 H40K133A10 has the largest value of *ACMR* among the frames compared, indicating that the  
 779 frame with the largest value of  $\eta$  has the lowest collapse risk. When the value of  $\eta$  is



780 increased from 0.30 to 0.35, the *ACMR* is increased by 1.5%. In addition, the value of *ACMR*  
781 for the H40K133A10 with  $\eta = 0.40$  is 1.61% higher than that of the H30K133A10 with  $\eta =$   
782 0.30. Thus, the collapse risk of the frames is reduced for higher values of  $\eta$ .

783 The frames examined here were compared in terms of their base factors  $\beta_{base}$  and  $\alpha$  to assess  
784 the effect of base stiffness on their collapse risk. For the frames with  $\eta=0.40$ , the following  
785 frames were compared to evaluate the effect of  $\beta_{base}$ , i.e.: H40K133A5 ( $\beta_{base}=133\%$ ) and  
786 H40K167A5 ( $\beta_{base}=167\%$ ), which have a value of  $\alpha=5\%$ ; H40K133A10 ( $\beta_{base}=133\%$ ) and  
787 H40K167A10 ( $\beta_{base}=167\%$ ), with  $\alpha=10\%$ ; and H40K133A15 ( $\beta_{base}=133\%$ ) and  
788 H40K167A15, with  $\alpha=15\%$ . For the frames with  $\eta=0.35$ , the following frames were  
789 compared: H35K133A5 ( $\beta_{base}=133\%$ ) and H35K167A5 ( $\beta_{base}=167\%$ ), with  $\alpha=5\%$ ;  
790 H35K133A10 ( $\beta_{base}=133\%$ ), H35K167A10 ( $\beta_{base}=167\%$ ) and H35K200A10 ( $\beta_{base}=200\%$ ),  
791 with  $\alpha=10\%$ ; and H35K133A15 ( $\beta_{base}=133\%$ ) and H35K167A15 ( $\beta_{base}=167\%$ ), with  $\alpha=15\%$ .

792 The results in Table 4 indicate that an increase of  $\beta_{base}$  from 133% to 167% results to higher  
793 values of *ACMR* for the frames with  $\eta=0.40$ . Thus, the increase of *ACMR* observed, due to  
794 the increase of  $\beta_{base}$ , is 1.63%, 0.46% and 1.21% for the design cases with  $\alpha$  equals 5%, 10%  
795 and 15%, respectively. Similar results are obtained for the frames with  $\eta=0.35$ . The values of  
796 *ACMR* of the frames with  $\beta_{base}$  equal to 167% are 3.40%, 0.12% and 0.29% higher than those  
797 of the frames with  $\beta_{base}$  equal to 133%, when  $\alpha$  equals 5%, 10% and 15%, respectively. In  
798 addition, the frame H35K200A10 ( $\beta_{base}=200\%$ ) has 1.46% and 1.58% higher values of  
799 *ACMR* than those of the H35K167A10 ( $\beta_{base}=167\%$ ) and H35K133A10 ( $\beta_{base}=133\%$ ),  
800 respectively. Thus, it can be concluded that the collapse resistance of the frames is increased  
801 for frames with higher values of  $\beta_{base}$ , representing the initial base stiffness.



802  
803

804  
805

Figure 13 Collapse fragility curves of SC-MRF, H35K133A5 and H35K200A10 for: (a) superior; (b) good; (c) fair; and (d) poor uncertainty rating.

806  
807  
808

809 For the design cases with  $\eta=0.40$ , the following frames were compared to evaluate the effect

810 of  $\alpha$ : H40K133A5 ( $\alpha=5\%$ ), H40K133A10 ( $\alpha=10\%$ ), H40K133A15 ( $\alpha=15\%$ ) and

811 H40K133A24 ( $\alpha=24.5\%$ ), with  $\beta_{base}=133\%$ ; and H40K167A5 ( $\alpha=5\%$ ), H40K167A10

812 ( $\alpha=10\%$ ) and H40K167A15 ( $\alpha=15\%$ ), with  $\beta_{base}=167\%$ . The results indicate that the higher

813 value of *ACMR* is achieved by H40K133A10 ( $\alpha=10\%$ ), for the frames with  $\beta_{base}=133\%$ .

814 Thus, collapse resistance of the frames is increased by 2.89% when  $\alpha$  increases from 5% to

815 10%, and is then reduced for further increase of  $\alpha$ . For the frames with  $\beta_{base}=167\%$  a different

816 trend is observed, with *ACMR* having higher values when  $\alpha$  increases. Thus, the frame

817 H40K167A15 ( $\alpha=15\%$ ) has 0.22% and 1.96% higher values of *ACMR* than those of

818 H40K167A10 ( $\alpha=10\%$ ) and H40K167A5 ( $\alpha=5\%$ ), respectively.

819 For the design cases with  $\eta=0.35$  the following frames were compared: H35K133A5 ( $\alpha=5\%$ ),  
820 H35K133A10 ( $\alpha=10\%$ ), H35K133A15 ( $\alpha=15\%$ ), and H35K133A20 ( $\alpha=20\%$ ), with  
821  $\beta_{base}=133\%$ ; and H35K167A5 ( $\alpha=5\%$ ), H35K167A10 ( $\alpha=10\%$ ) and H35K167A15 ( $\alpha=15\%$ ),  
822 with  $\beta_{base}=167\%$ . The results of the frames with  $\beta_{base}=133\%$  demonstrate that the *ACMR* is  
823 increased when  $\alpha$  is increased from 5% to 15% and is then reduced for further increase of  $\alpha$ .  
824 A similar trend is observed for the frames with  $\beta_{base}=167\%$ .

## 825 **8 CONCLUSIONS**

826 The potential of the SC-MRF-CBs to improve the seismic performance and reduce the  
827 collapse risk of earthquake-resilient steel buildings with SC-MRFs was examined. The effect  
828 of strength and stiffness characteristics of the novel self-centering column base to improve  
829 the seismic performance and collapse capacity of the SC-MRF-CBs was also investigated.  
830 The parameters through which these effects were taken into consideration were three  
831 normalised factors that represent the initial stiffness, post-yield stiffness and strength of the  
832 self-centering column bases. These structural properties of the self-centering column bases  
833 can be independently adjusted by utilising the analytical expressions that are presented in this  
834 research, thereby changing also the initial stiffness, post-yield stiffness and strength of the  
835 whole SC-MRF-CBs. A design procedure for the self-centering column bases, which is  
836 enhanced compared to that in [29], is also proposed to that purpose. The evaluation of the  
837 seismic performance and collapse risk of the SC-MRF-CBs was based on a prototype steel  
838 building designed to incorporate different seismic-resistant frames, i.e., one SC-MRF and  
839 sixteen SC-MRF-CBs' designs with different base stiffness and strength characteristics. A set  
840 of 44 ground motions that were scaled to three seismic intensity levels was utilised to  
841 perform non-linear dynamic analyses and evaluate the seismic performance of the frames.  
842 Moreover, IDA was used with the same set of ground motions to evaluate the collapse

843 capacity of the frames. Finally, fragility curves and the *ACMR* of the frames were derived to  
844 compare their seismic risk.

845 On the basis of the findings of this paper, the following conclusions can be drawn:

- 846 1. The SC-MRF-CBs have in general better seismic performance than the SC-MRF in  
847 terms of  $\theta_{s,max}$  and PFA. The results demonstrate that the self-centering column base  
848 is very effective in reducing  $\theta_{s,max}$  and PFA, by only tuning its base stiffness and  
849 strength characteristics. Thus, non-structural elements and equipment installed to SC-  
850 MRF-CBs will potentially exhibit less damage. A potential of reducing the cross-  
851 sections of the members of the SC-MRF-CBs can be also concluded. That is because  
852 the SC-MRF-CBs exhibit  $\theta_{s,max}$  values lower than the relevant limits of EC8 under the  
853 FOE, DBE and MCE. This reduction reaches an appreciable 24.05%.
- 854 2. The H35K133A5 and H35K200A10 (i.e., the two frames that exhibit the lowest and  
855 highest values of  $\theta_{s,res}$  among the investigated SC-MRF-CBs) have lower values of  
856  $\theta_{s,res}$  in all their storeys, compared to those of the SC-MRF. These values are almost  
857 negligible and are solely due to permanent deformations in the PT beam-column  
858 connections since the self-centering column bases behave elastically up to their  
859 targeted rotations.
- 860 3. The SC-MRF-CBs have superior collapse capacity compared to the SC-MRF. The  
861 collapse capacity and *ACMR* of the SC-MRF-CBs are increased by up to 33.23% and  
862 27.95%, respectively, compared to the SC-MRF.
- 863 4. The collapse risk of the SC-MRF-CBs is reduced for higher values of  $\eta$ . The  
864 H40K133A10 with  $\eta=0.40$  has the largest value of *ACMR* and thus the lowest  
865 collapse risk compared to the frames with  $\eta$  equal to 0.35 and 0.30.
- 866 5. It is concluded that collapse capacity of the frames is increased for frames with higher  
867 values of  $\beta_{base}$ . The SC-MRF-CBs with  $\beta_{base}=167\%$  have superior collapse resistance

868 than the ones with  $\beta_{base}=133\%$ , when  $\eta=0.40$ . The maximum increase of *ACMR*  
869 observed, due to the increase of  $\beta_{base}$ , is 1.63% for the design cases with  $\alpha=5\%$ .  
870 Similar results are obtained for the frames with  $\eta=0.35$ . The values of *ACMR* of the  
871 frames with  $\beta_{base}=167\%$  are 3.40%, 0.12% and 0.29% higher than those of the frames  
872 with  $\beta_{base}=133\%$ , when  $\alpha$  equals 5%, 10% and 15%, respectively. In addition, the  
873 frame H35K200A10 ( $\beta_{base}=200\%$ ) has 1.46% and 1.58% higher values of *ACMR* than  
874 those of the H35K167A10 ( $\beta_{base}=167\%$ ) and H35K133A10 ( $\beta_{base}=133\%$ ),  
875 respectively.

876 6. The results for the SC-MRF-CBs with  $\eta=0.40$  indicate that the higher value of *ACMR*  
877 is achieved by the frame with  $\alpha=10\%$ , for the frames with  $\beta_{base}=133\%$ . Thus, the  
878 collapse capacity of the frames increases by 2.89% when  $\alpha$  increases from 5% to 10%  
879 and is then reduced for further increase of  $\alpha$ . For the frames with  $\beta_{base}=167\%$ , a  
880 different trend is observed, with *ACMR* having higher values when  $\alpha$  is increased up  
881 to 15%.

882 7. For the SC-MRF-CBs with  $\eta=0.35$  and  $\beta_{base}=133\%$ , it is observed that the *ACMR* is  
883 increased when  $\alpha$  is increased from 5% to 15% and is then reduced for further  
884 increase of  $\alpha$ . A similar trend is observed for the frames with  $\beta_{base}=167\%$ . Thus, an  
885 increase of  $\alpha$  up to a certain value leads to an increase of the collapse capacity of the  
886 frames. It is also concluded that  $\alpha$  is more effective in increasing the collapse capacity  
887 of the frames compared to  $\beta_{base}$ , because a similar increase of the collapse capacity is  
888 achieved by increasing both parameters, but for a larger increase of  $\beta_{base}$ .

889 8. It is concluded that the best seismic performance and highest collapse capacity among  
890 the SC-MRF-CBs examined is achieved for a combination of the strength factor,  $\eta$ ,  
891 equal to 0.35; initial stiffness factor,  $\beta_{base}$ , equal to 200%; and post-yield stiffness  
892 ratio,  $\alpha$ , equal to 10%.

## 893 REFERENCES

- 894 [1] H. Inamasu, D.G. Lignos, A.M. Kanvinde, Effect of column base flexibility on the  
895 hysteretic response of wide flange steel columns, 3rd Huixian Int. Forum Earthq. Eng.  
896 Young Res. August 11-12. (2017) Paper No. 260.  
897 [https://infoscience.epfl.ch/record/230104/files/260\\_Inamasu\\_Hiroyuki\\_fullpaper.pdf](https://infoscience.epfl.ch/record/230104/files/260_Inamasu_Hiroyuki_fullpaper.pdf).
- 898 [2] F. Zareian, A. Kanvinde, Effect of column-base flexibility on the seismic response and  
899 safety of steel moment-resisting frames, *Earthq. Spectra*. 29 (2013) 1537–1559.  
900 doi:10.1193/030512EQS062M.
- 901 [3] J. Ruiz-García, A. Kanvinde, Effect of column base flexibility on residual drift  
902 demands of low-rise steel moment-resisting frames, in: 2013 World Congr. Adv.  
903 Struct. Eng. Eng. Mech. (ASEM13), Sept. 8-12, Jeju, Korea, 2013: pp. 627–639.
- 904 [4] P.A. Torres-Rodas, F. Flores, F. Zareian, Seismic response of steel moment frame  
905 considering gravity system and column base flexibility, in: Proc. 11th US Natl. Conf.  
906 Earthq. Eng., June 25-29, Los Angeles, USA, 2018.  
907 [https://www.researchgate.net/profile/Pablo\\_Torres-](https://www.researchgate.net/profile/Pablo_Torres-Rodas/publication/327663389_Seismic_Response_of_Steel_Moment_Frames_considering_gravity_system_and_column_base_flexibility/links/5b9c618292851ca9ed0aa655/Seismic-Response-of-Steel-Moment-Frames-considering)  
908 [Rodas/publication/327663389\\_Seismic\\_Response\\_of\\_Steel\\_Moment\\_Frames\\_considering\\_gravity\\_system\\_and\\_column\\_base\\_flexibility/links/5b9c618292851ca9ed0aa655/](https://www.researchgate.net/profile/Pablo_Torres-Rodas/publication/327663389_Seismic_Response_of_Steel_Moment_Frames_considering_gravity_system_and_column_base_flexibility/links/5b9c618292851ca9ed0aa655/Seismic-Response-of-Steel-Moment-Frames-considering)  
909 [Seismic-Response-of-Steel-Moment-Frames-considering](https://www.researchgate.net/profile/Pablo_Torres-Rodas/publication/327663389_Seismic_Response_of_Steel_Moment_Frames_considering_gravity_system_and_column_base_flexibility/links/5b9c618292851ca9ed0aa655/Seismic-Response-of-Steel-Moment-Frames-considering).
- 911 [5] A. Aviram, B. Stojadinovic, A. Der Kiureghian, Performance and reliability of  
912 exposed column base plate connections for steel moment-resisting frames, Berkeley,  
913 CA, USA, 2010.
- 914 [6] BS EN 1998-1, Eurocode 8: Design of structures for earthquake resistance - Part 1:  
915 General rules, seismic actions and rules for buildings., 2013.
- 916 [7] P.T. Rodas, F. Zareian, A. Kanvinde, Hysteretic Model for Exposed Column–Base  
917 Connections, *J. Struct. Eng.* (2016) 04016137. doi:10.1061/(ASCE)ST.1943-  
918 541X.0001602.
- 919 [8] D.G. Lignos, H. Krawinkler, A database in support of modeling of component  
920 deterioration for collapse prediction of steel frame structures, in: John W. Wallace  
921 (Ed.), *Struct. Eng. Res. Front.* May 16-19, Long Beach, California, United States,  
922 2007: pp. 1–12. doi:doi: 10.1061/40944(249)31.
- 923 [9] H.-J. Kim, C. Christopoulos, Seismic design procedure and seismic response of post-  
924 tensioned self-centering steel frames, *Earthquake Eng. Struct. Dyn.* 38 (2009) 355–  
925 376. doi:10.1002/eqe.859.
- 926 [10] A.S. Tzimas, A.I. Dimopoulos, T.L. Karavasilis, EC8-based seismic design and  
927 assessment of self-centering steel frames with viscous dampers, *J. Constr. Steel Res.*  
928 105 (2015) 60–73.
- 929 [11] J.M. Ricles, R. Sause, M.E.M. Garlock, C. Zhao, Posttensioned seismic-resistant  
930 connections for steel frames, *J. Struct. Eng.* 127 (2001) 113–121.
- 931 [12] K.-C. Tsai, C.-C. Chou, C.-L. Lin, P.-C. Chen, S.-J. Jhang, Seismic self-centering steel  
932 beam-to-column moment connections using bolted friction devices, *Earthq. Eng.*  
933 *Struct. Dyn.* 37 (2008) 627–645. doi:10.1002/eqe.779.
- 934 [13] G. Vasdravellis, T.L. Karavasilis, B. Uy, Large-scale experimental validation of steel  
935 post-tensioned connections with web hourglass pins, *J. Struct. Eng.* 139 (2013) 1033–  
936 42. doi:10.1061/(ASCE)ST.1943-541X.0000696.
- 937 [14] G. Vasdravellis, T.L. Karavasilis, B. Uy, Design rules, experimental evaluation, and  
938 fracture models for high-strength and stainless-steel hourglass shape energy dissipation  
939 devices, *J. Struct. Eng.* 140 (2014) 04014087. doi:10.1061/(ASCE)ST.1943-  
940 541X.0001014.
- 941 [15] P. Rojas, J.M. Ricles, R. Sause, Seismic Performance of Post-tensioned Steel Moment

- 942 Resisting Frames with Friction Devices, *J. Struct. Eng.* 131 (2005) 529–540.  
 943 doi:10.1061/(ASCE)0733-9445(2005)131:4(529).
- 944 [16] C.-C. Chou, Y.-C. Wang, J.-H. Chen, Seismic design and behavior of post-tensioned  
 945 steel connections including effects of a composite slab, *Eng. Struct.* 30 (2008) 3014–  
 946 3023. doi:10.1016/j.engstruct.2008.04.013.
- 947 [17] M.A. Chowdhury, A. Rahmzadeh, M.S. Alam, Improving the seismic performance of  
 948 post-tensioned self-centering connections using SMA angles or end plates with SMA  
 949 bolts, *Smart Mater. Struct.* 28 (2019) 075044.
- 950 [18] M.A. Chowdhury, A. Rahmzadeh, S. Moradi, M.S. Alam, Feasibility of using reduced  
 951 length superelastic shape memory alloy strands in post-tensioned steel beam–column  
 952 connections, *J. Intell. Mater. Syst. Struct.* 30 (2018) 283–307.  
 953 doi:10.1177/1045389X18806393.
- 954 [19] B. Uy, Innovative connections for the demountability and rehabilitation of steel, space  
 955 and composite structures, in: 12th Int. Conf. Steel, Sp. Compos. Struct. 28-30 May,  
 956 Prague, Czech Republic, 2014: pp. 99–109.
- 957 [20] J. Liu, Design for Deconstruction with Demountable Composite Beams and Floor  
 958 Systems, *Eng. J.* 53 (2016) 107–16.
- 959 [21] S. Pampanin, C. Christopoulos, M.J.N. Priestley, Performance-based seismic response  
 960 of frame structures including residual deformations. Part II: Multi-degree of freedom  
 961 systems., *J. Earthq. Eng.* 7 (2003) 119–147.
- 962 [22] C. Christopoulos, A. Filiatrault, B. Folz, Seismic response of self-centring hysteretic  
 963 SDOF systems, *Earthq. Eng. Struct. Dyn.* 31 (2002) 1131–1150. doi:10.1002/eqe.152.
- 964 [23] C. Christopoulos, Frequency Response of Flag-Shaped Single Degree-of-Freedom  
 965 Hysteretic Systems, *J. Eng. Mech.* 130 (2004) 894–903. doi:10.1061/(ASCE)0733-  
 966 9399(2004)130:8(894).
- 967 [24] C. Christopoulos, S. Pampanin, M.J.N. Priestley, Performance-based seismic response  
 968 of frame structures including residual deformations. Part 1: Single-degree of freedom  
 969 systems., *J. Earthq. Eng.* 7 (2003) 97–118.
- 970 [25] T.L. Karavasilis, C.-Y. Seo, Seismic structural and non-structural performance  
 971 evaluation of highly damped self-centering and conventional systems, *Eng. Struct.* 33  
 972 (2011) 2248–2258. doi:10.1016/j.engstruct.2011.04.001.
- 973 [26] G.P. Cimellaro, Simultaneous stiffness–damping optimization of structures with  
 974 respect to acceleration, displacement and base shear, *Eng. Struct.* 29 (2007) 2853–  
 975 2870. doi:10.1016/j.engstruct.2007.01.001.
- 976 [27] C.-C. Chou, J.-H. Chen, Analytical model validation and influence of column bases for  
 977 seismic responses of steel post-tensioned self-centering MRF systems, *Eng. Struct.* 33  
 978 (2011) 2628–2643. doi:10.1016/j.engstruct.2011.05.011.
- 979 [28] BS EN 1998-3, Eurocode 8 : Design of structures for earthquake resistance — Part 3:  
 980 Assessment and retrofitting of buildings., 2005.
- 981 [29] V.C. Kamperidis, T.L. Karavasilis, G. Vasdravellis, Self-centering steel column base  
 982 with metallic energy dissipation devices, *J. Constr. Steel Res.* 149 (2018) 14–30.  
 983 doi:10.1016/j.jcsr.2018.06.027.
- 984 [30] H. Chi, J. Liu, Seismic behavior of post-tensioned column base for steel self-centering  
 985 moment resisting frame, *J. Constr. Steel Res.* 78 (2012) 117–130.  
 986 doi:10.1016/j.jcsr.2012.07.005.
- 987 [31] X.-T. Wang, C.-D. Xie, L.-H. Lin, J. Li, Seismic behavior of self-centering concrete-  
 988 filled square steel tubular (CFST) Column Base, *J. Constr. Steel Res.* 156 (2019) 75–  
 989 85. doi:https://doi.org/10.1016/j.jcsr.2019.01.025.
- 990 [32] M. Latour, G. Rizzano, A. Santiago, L. Simões da Silva, Experimental response of a  
 991 low-yielding, self-centering, rocking column base joint with friction dampers, *Soil*

- 992 Dyn. Earthq. Eng. 116 (2019) 580–592.  
 993 doi:<https://doi.org/10.1016/j.soildyn.2018.10.011>.
- 994 [33] B. Wang, S. Zhu, C.-X. Qiu, H. Jin, High-performance self-centering steel columns  
 995 with shape memory alloy bolts: Design procedure and experimental evaluation, *Eng.*  
 996 *Struct.* 182 (2019) 446–458. doi:<https://doi.org/10.1016/j.engstruct.2018.12.077>.
- 997 [34] FEMA, FEMA P-58-1 Seismic performance assessment of buildings - Volume 1 -  
 998 Methodology (2nd Edition), Washington, DC, USA, 2018.  
 999 <https://www.fema.gov/media-library/assets/documents/90380>.
- 1000 [35] A.S. Tzimas, G.S. Kamaris, T.L. Karavasilis, C. Galasso, Collapse risk and residual  
 1001 drift performance of steel buildings using post-tensioned MRFs and viscous dampers  
 1002 in near-fault regions, *Bull. Earthq. Eng.* 14 (2016) 1643–1662. doi:10.1007/s10518-  
 1003 016-9898-3.
- 1004 [36] A.I. Dimopoulos, T.L. Karavasilis, G. Vasdravellis, B. Uy, Seismic design, modelling  
 1005 and assessment of self-centering steel frames using post-tensioned connections with  
 1006 web hourglass shape pins, *Bull. Earthq. Eng.* 11 (2013) 1797–1816.  
 1007 doi:10.1007/s10518-013-9437-4.
- 1008 [37] ASTM, ASTM A416/A416M-05, Standard Specification for Steel Strand, Uncoated  
 1009 Seven-Wire for Prestressed Concrete, West Conshohocken, PA, USA, 2005.
- 1010 [38] T.L. Bruce, M.R. Eatherton, Behavior of Post-Tensioning Strand Systems Subjected to  
 1011 Inelastic Cyclic Loading, *J. Struct. Eng.* 142 (2016) 04016067.  
 1012 doi:10.1061/(ASCE)ST.1943-541X.0001503.
- 1013 [39] P. Sideris, A.J. Aref, A. Filiatrault, Effects of anchorage hardware on the cyclic tensile  
 1014 response of unbonded monostrands, *PCI J.* 59 (2014) 60–77.  
 1015 doi:10.15554/pcij.06012014.60.77.
- 1016 [40] G.A. MacRae, C.R. Urmson, W.R. Walpole, P. Moss, K. Hyde, C. Clifton, Axial  
 1017 shortening of steel columns in buildings subjected to earthquakes, *Bull. New Zeal.*  
 1018 *Soc. Earthq. Eng.* 42 (2009) 275–287.
- 1019 [41] R. Vargas, M. Bruneau, Analytical Response and Design of Buildings with Metallic  
 1020 Structural Fuses. I, *J. Struct. Eng.* 135 (2009) 386–93. doi:10.1061/(ASCE)0733-  
 1021 9445(2009)135:4(386).
- 1022 [42] Y.-C. Lin, R. Sause, J.M. Ricles, Seismic Performance of a Large-Scale Steel Self-  
 1023 Centering Moment-Resisting Frame: MCE Hybrid Simulations and Quasi-Static  
 1024 Pushover Tests, *J. Struct. Eng.* 139 (2013) 1227–1236. doi:10.1061/(ASCE)ST.1943-  
 1025 541X.0000661.
- 1026 [43] T.C. Steele, L.D.A. Wiebe, Collapse risk of controlled rocking steel braced frames  
 1027 with different post-tensioning and energy dissipation designs, *Earthq. Eng. Struct.*  
 1028 *Dyn.* (2017). doi:10.1002/eqe.2892.
- 1029 [44] BS EN 1993-1-1, Eurocode 3: Design of steel structures - Part 1-1: General rules and  
 1030 rules for steel buildings, United Kingdom, 2009.
- 1031 [45] BS EN 1993-1-8, Eurocode 3 : Design of steel structures — Part 1-8 : Design of joints,  
 1032 United Kingdom, 2010.
- 1033 [46] L. Wiebe, C. Christopoulos, Performance-Based Seismic Design of Controlled  
 1034 Rocking Steel Braced Frames. I: Methodological Framework and Design of Base  
 1035 Rocking Joint, *J. Struct. Eng.* 141 (2015). doi:10.1061/(ASCE)ST.1943-  
 1036 541X.0001202.
- 1037 [47] G. Vasdravellis, T.L. Karavasilis, B. Uy, Finite element models and cyclic behavior of  
 1038 self-centering steel post-tensioned connections with web hourglass pins, *Eng. Struct.*  
 1039 52 (2013) 1–16. doi:<http://dx.doi.org/10.1016/j.engstruct.2013.02.005>.
- 1040 [48] U. of C. Pacific Earthquake Engineering Research Center (PEER), OpenSees, (2015).  
 1041 <http://opensees.berkeley.edu>.



- 1042 [49] M.H. Scott, G.L. Fenves, Plastic hinge integration methods for force-based beam-  
 1043 column elements, *J. Struct. Eng.* 132 (2006) 244–252.
- 1044 [50] D.G. Lignos, H. Krawinkler, Deterioration Modeling of Steel Components in Support  
 1045 of Collapse Prediction of Steel Moment Frames under Earthquake Loading, *J. Struct.*  
 1046 *Eng.* 137 (2011) 1291–1302. doi:10.1061/(ASCE)ST.1943-541X.0000376.
- 1047 [51] M. Hamidia, A. Filiatrault, A.J. Aref, Simplified seismic sidesway collapse analysis of  
 1048 frame buildings, *Earthq. Eng. Struct. Dyn.* 43 (2014) 429–448. doi:10.1002/eqe.2353.
- 1049 [52] H. Krawinkler, Shear in Beam-Column Joints in Seismic Design of Frames, *Eng. J.* 15  
 1050 (1978).
- 1051 [53] C.C. Chou, K.C. Tsai, W.C. Yang, Self-centering steel connections with steel bars and  
 1052 a discontinuous composite slab, *Earthq. Eng. Struct. Dyn.* 38 (2009) 403–422.  
 1053 doi:10.1002/eqe.856.
- 1054 [54] G. Vasdravellis, M. Baiguera, D. Al-Sammarai, Robustness assessment of a steel self-  
 1055 centering moment-resisting frame under column loss, *J. Constr. Steel Res.* 141 (2018)  
 1056 36–49. doi:10.1016/j.jcsr.2017.11.004.
- 1057 [55] M. Bruneau, C.-M. Uang, R. Sabelli, Ductile design of steel structures, Second Edi,  
 1058 McGraw-Hill Education, 2011.
- 1059 [56] P. Uriz, Towards Earthquake Resistant Design of Concentrically Braced Steel  
 1060 Structures, University of California, Berkeley, USA, 2005.
- 1061 [57] VSL International Ltd, Post-tensioning, stay cables & construction methods, Prod.  
 1062 Broch. VSL STRAND POST-TENSIONING Syst. (2013). www.vsl.com.
- 1063 [58] M. Baiguera, G. Vasdravellis, T.L. Karavasilis, Ultralow Cycle Fatigue Tests and  
 1064 Fracture Prediction Models for Duplex Stainless-Steel Devices of High Seismic  
 1065 Performance Braced Frames, *J. Struct. Eng.* 145 (2019) 04018230.  
 1066 doi:10.1061/(ASCE) ST.1943-541X.0002243.
- 1067 [59] FEMA, Quantification of building seismic performance factors (FEMA P695) (ATC-  
 1068 63 Project), USA, 2009. [https://www.fema.gov/media-library-data/20130726-1716-  
 1069 25045-9655/fema\\_p695.pdf](https://www.fema.gov/media-library-data/20130726-1716-25045-9655/fema_p695.pdf).
- 1070 [60] ASCE/SEI, Seismic rehabilitation of existing buildings (ASCE/SEI 41-06), U.S.A.,  
 1071 2007.
- 1072 [61] L.T. Kibriya, C. Málaga-Chuquitaype, M.M. Kashani, N.A. Alexander, Nonlinear  
 1073 dynamics of self-centring rocking steel frames using finite element models, *Soil Dyn.*  
 1074 *Earthq. Eng.* 1115 (2018) 826–37. doi:<https://doi.org/10.1016/j.soildyn.2018.09.036>.
- 1075 [62] J. McCormick, H. Aburano, M. Ikenaga, M. Nakashima, Permissible Residual  
 1076 Deformation Levels for Building Structures Considering both Safety and Human  
 1077 Elements, in: 14th World Conf. Earthq. Eng. Oct. 12-17, China Earthquake  
 1078 Administration Ministry of Construction, Beijing, China, 2008.
- 1079 [63] D. Vamvatsikos, C.A. Cornell, Incremental dynamic analysis, *Earthq. Eng. Struct.*  
 1080 *Dyn.* 31 (2002) 491–514. doi:10.1002/eqe.141.
- 1081 [64] C.Y. Seo, T.L. Karavasilis, J.M. Ricles, R. Sause, Seismic performance and  
 1082 probabilistic collapse resistance assessment of steel moment resisting frames with fluid  
 1083 viscous dampers, *Earthq. Eng. Struct. Dyn.* 43 (2014) 2059–2216.  
 1084 doi:10.1002/eqe.2440.
- 1085 [65] J.W. Baker, C.A. Cornell, Spectral shape, epsilon and record selection, *Earthq. Eng.*  
 1086 *Struct. Dyn.* 35 (2006) 1077–95. doi:10.1002/eqe.571.
- 1087